



# Microwave-assisted molten-salt rapid synthesis of isotype triazine-/heptazine based g-C<sub>3</sub>N<sub>4</sub> heterojunctions with highly enhanced photocatalytic hydrogen evolution performance



Huanhuan Liu<sup>a</sup>, Deliang Chen (Professor)<sup>a,b,\*</sup>, Zhiqiang Wang<sup>a</sup>, Huijuan Jing<sup>a</sup>, Rui Zhang<sup>a,c</sup>

<sup>a</sup> School of Materials Science and Engineering, Zhengzhou University, Zhengzhou 450001, China

<sup>b</sup> School of Chemical Engineering and Energy Technology, Dongguan University of Technology, Dongguan 523808, China

<sup>c</sup> Laboratory of Aeronautical Composites, Zhengzhou Institute of Aeronautical Industry Management, Zhengzhou 450046, China

## ARTICLE INFO

### Article history:

Received 27 July 2016

Received in revised form 2 September 2016

Accepted 8 October 2016

Available online 15 October 2016

### Keywords:

Graphitic carbon nitride

Isotype g-C<sub>3</sub>N<sub>4</sub>/g-C<sub>3</sub>N<sub>4</sub> heterojunction

Microwave-assisted molten-salt synthesis

Photocatalytic hydrogen evolution

Thermo-polymerization of melamine

## ABSTRACT

Rapid synthesis and construction of graphitic carbon nitride (g-C<sub>3</sub>N<sub>4</sub>) based heterojunctions, cost-effective metal-free photocatalysts for hydrogen evolution reaction (HER) under solar irradiation, is of highly practical significance. This work reports a one-pot microwave-assisted molten-salt (mw-ms) process to rapidly synthesize isotype triazine-/heptazine based g-C<sub>3</sub>N<sub>4</sub> heterojunctions with highly enhanced photocatalytic HER performance using melamine as the single-source precursor. The typical sample (mw-ms-g-C<sub>3</sub>N<sub>4</sub>) was obtained by thermally polymerizing melamine molecules at 550 °C for 30 min in the media of eutectic KCl/LiCl salts under microwave irradiation in air. The analyses of phases, chemical compositions and microstructures indicate that the mw-ms-g-C<sub>3</sub>N<sub>4</sub> sample consists of an isotype triazine-/heptazine based g-C<sub>3</sub>N<sub>4</sub> heterojunction, taking on a plate-like morphology with a specific surface area ( $S_{BET}$ ) of 25.7 m<sup>2</sup> g<sup>-1</sup>. Comparatively, the g-C<sub>3</sub>N<sub>4</sub> sample synthesized via an electric-resistance molten-salt (er-ms) process at 550 °C for 240 min is composed of a triazine-based g-C<sub>3</sub>N<sub>4</sub> phase with a  $S_{BET}$  of 58.1 m<sup>2</sup> g<sup>-1</sup>, whereas the samples obtained by electric-resistance heating (er, at 550 °C for 240 min) and microwave heating (mw, at 550 °C for 30 min) processes consist of a heptazine-based g-C<sub>3</sub>N<sub>4</sub> phase. The mw-ms-g-C<sub>3</sub>N<sub>4</sub> sample shows a photocatalytic HER rate of 1480 μmol g<sup>-1</sup> h<sup>-1</sup>, which is 5 times that (300 μmol g<sup>-1</sup> h<sup>-1</sup>) of the er-ms-g-C<sub>3</sub>N<sub>4</sub> sample, 15 times that (95 μmol g<sup>-1</sup> h<sup>-1</sup>) of the er-g-C<sub>3</sub>N<sub>4</sub> sample and 23 times that (63 μmol g<sup>-1</sup> h<sup>-1</sup>) of the mw-g-C<sub>3</sub>N<sub>4</sub> sample, under the similar visible-light ( $\lambda \geq 420$  nm) irradiation. The typical apparent quantum yield of the mw-ms-g-C<sub>3</sub>N<sub>4</sub> sample at 420 nm is up to 10.7%. The UV-vis DR spectra suggest that both the triazine-based g-C<sub>3</sub>N<sub>4</sub> and heptazine-based g-C<sub>3</sub>N<sub>4</sub> phases have a similar bandgap of ~2.66 eV, whereas the Mott-Schottky analysis indicates that the triazine-based g-C<sub>3</sub>N<sub>4</sub> phase has a more positive flat conductive potential (-0.90 V) than the triazine-based g-C<sub>3</sub>N<sub>4</sub> phase (-1.22 V). Due to the suitable alignment of their energy bandgap structures, the isotype triazine-/heptazine based g-C<sub>3</sub>N<sub>4</sub> hybrids in the mw-ms-g-C<sub>3</sub>N<sub>4</sub> sample form a type II heterojunction of semiconductor/semiconductor, which provides a convenient carrier transfer path and leads to more efficient separation of photo-generated electron-hole pairs than the other samples. The synergistic effects of microwave heating and molten-salt liquid polycondensation provide a robust platform for rapid and large-scale construction of isotype g-C<sub>3</sub>N<sub>4</sub>/g-C<sub>3</sub>N<sub>4</sub> heterojunctions as metal-free high-performance HER photocatalysts using a simple single-source precursor.

© 2016 Elsevier B.V. All rights reserved.

## 1. Introduction

Hydrogen is a kind of clean energy, and photocatalytic water splitting for hydrogen evolution is a promising strategy to relieve increasing concern over the depletion of fossil fuels which are tightly associated with energy issues and pollution problems [1]. Though tremendous photocatalysts have been developed as water-

\* Corresponding author at: School of Materials Science and Engineering, Zhengzhou University, Zhengzhou, 450001, China.

E-mail addresses: [dlchen@zzu.edu.cn](mailto:dlchen@zzu.edu.cn), [dlchennano@qq.com](mailto:dlchennano@qq.com), [dlchennano@hotmail.com](mailto:dlchennano@hotmail.com) (D. Chen).

splitting photocatalysts [2], some problems, such as complicated synthetic process, high cost and low utilization of solar light, still hinder the commercial applications of these photocatalysts [3,4]. To date, to develop novel photocatalysts with excellent and stable performance is still a challengeable task.

Recently, graphitic carbon nitride ( $\text{g-C}_3\text{N}_4$ ), a polymeric visible-light photocatalyst, has drawn increasing attention because of its suitable electric band-gap and efficient photocatalytic hydrogen evolution reaction (HER) activity [5,6]. Basically, the framework of  $\text{g-C}_3\text{N}_4$  is composed of two basic tectonic units: one is the s-triazine ring and the other is the tri-s-triazine (or heptazine) ring which consists of three s-triazine rings connected by central N atoms [6,7]. As a typical metal-free photocatalyst, graphitic carbon nitride is beneficial from many aspects, e.g., plenty and low-cost precursors [8], excellent optical properties [9], and easy preparation [10]. However, for the  $\text{g-C}_3\text{N}_4$  photocatalysts, the low separation efficiency of photogenerated electron-hole carries and their poor transfer ability are still obstacles for their practical applications. Also, the conventional thermal polycondensation of C, N-containing precursors is a time-consuming and low cost-effective process.

To further improve the performance of  $\text{g-C}_3\text{N}_4$  photocatalysts, many scientists have developed multifarious strategies based on different principles, e.g., adjusting microstructures [11–14], forming defects [15–17], doping [18–20], forming heterojunctions [21–25], and adding carbon species [26–28]. These modification strategies mainly focus on shortening the distance of transfer paths, forming unique transmission channels or supporting more active sites for trapping carriers, and facilitating the separation and transmission of photogenerated electron-hole pairs. Band-alignment design for  $\text{g-C}_3\text{N}_4$  photocatalysts, usually obtained by the traditional thermal polycondensation method, is an effective approach to enhance the separation and transmission of photogenerated carriers by forming nano-junctions at the interfaces. Compared to the heterojunctions constructed with the second-phase metals or semiconductors, the ones with isotype  $\text{g-C}_3\text{N}_4$  phases are more fascinating. Wang et al. have reported a CNS-CN isotype heterojunction via a two-step thermal treating process, and the resultant sample was of excellent photocatalytic watersplitting performance [29]. Besides, the  $\text{g-C}_3\text{N}_4$  isotype heterostructure has also been prepared by thermal polymerization of the mixed precursor of urea and thiourea [25]. However, there is still a big challenge to synthesize  $\text{g-C}_3\text{N}_4$  isotype heterojunctions for HER photocatalysts from a single-source precursor (i.e., melamine) via a simple process.

Recently, some new strategies have been devolved to synthesize  $\text{g-C}_3\text{N}_4$  based photocatalysts. For example, molten salts, unique high-temperature ionic liquids, have been used as the media to prepare polymeric carbon nitrides [30]. Schwinghammer et al. [31] have developed an electric-resistance heating molten-salt method to synthesize poly(triazine imide) (PTI) photocatalysts (i.e., triazine-based  $\text{g-C}_3\text{N}_4$ ) with enhanced  $\text{H}_2$  evolution performance. The above triazine-based  $\text{g-C}_3\text{N}_4$  is an isotype of the heptazine-based  $\text{g-C}_3\text{N}_4$  obtained by conventional electric-resistance thermal methods. Taking advantage of the molten-salt method, researchers can use templates [32], various precursors [33] and secondary semiconductors [34] to construct novel carbon nitride based photocatalysts. Besides  $\text{g-C}_3\text{N}_4$ , the molten-salt method has also been used to prepare other functional materials, e.g., graphitic carbon [35] and graphene [36]. The molten-salt process offers a unique liquid condition that is stable and convenient for high-temperature synthesis [37]. Though the electric-resistance heating molten-salt method can be used to synthesize high-performance graphitic carbon nitride photocatalysts, the problems of time consuming in synthesis and low efficiency in performance are still difficult to overcome.

Microwave irradiation, known as an efficient heating manner, benefits from its ultrafast heating rate due to dipolar polariza-

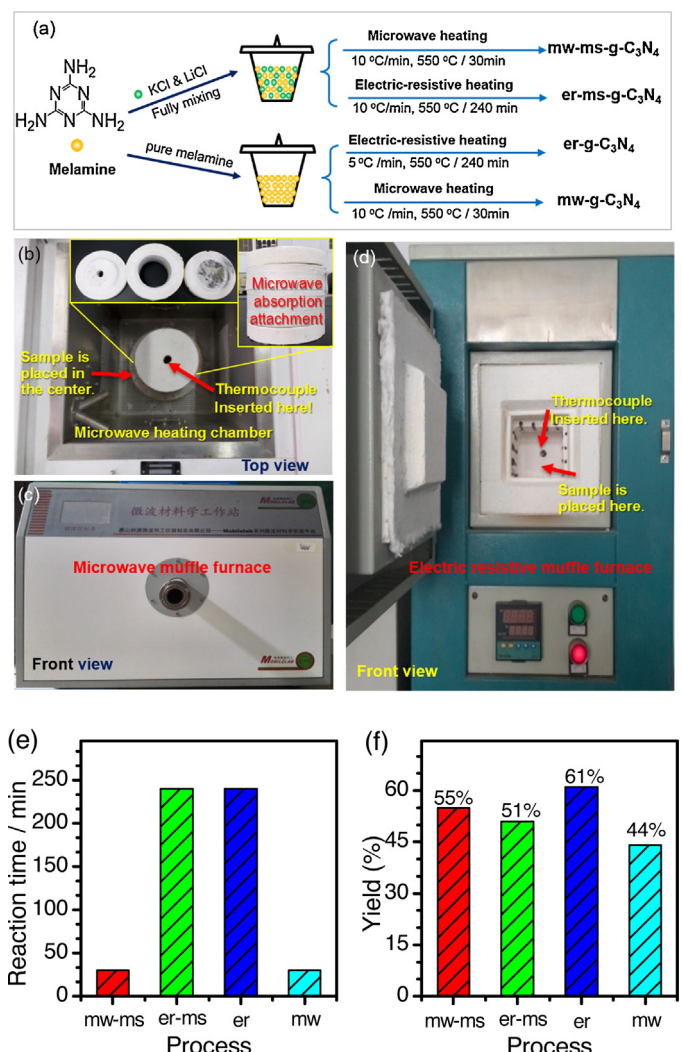


**Fig. 1.** Schematic illustration of the synthetic processes for graphitic carbon nitride photocatalysts from melamine: (a) Typical 4 thermal polymerization processes (mw-ms=microwave-assisted molten-salt process, er-ms=electric-resistance molten-salt process, er=electric-resistance heating, and mw=microwave-heating process); (b–c) Structure of the microwave workstation used; (d) Structure of the electric-resistance furnace used; (e) Comparison of polymerization times for various processes; (f) Comparison of typical yields of graphitic carbon nitride photocatalysts via the different processes.

tion or ionic conduction [38]. Yuan et al. [39] have reported a microwave-assisted heating method to synthesize a highly crystalline  $\text{g-C}_3\text{N}_4$  photocatalyst in a few minutes, suggesting that the microwave heating is a potential way in rapid synthesis of carbon nitride based materials. To achieve a stable and reliable condition in a solid-state reaction system, many measures have to be considered under microwave irradiation, whereas the liquid reaction condition can provide a more stable microwave heating process [40]. Therefore, multifarious liquid phases, e.g., aqueous solutions [41], polyols [42] and ionic liquids [43], have been used as reaction media in the microwave-assisted processes to improve the stability of microwave heating.

We herein develop a microwave-assisted molten-salt (mw-ms) process to synthesize an isotype heterojunction of triazine-/heptazine based  $\text{g-C}_3\text{N}_4$  photocatalysts using easily available melamine as the single-source precursor. This process combines the advantages of rapid heating of microwave irradiation and high-temperature liquid media of molten-salt KCl/LiCl mixtures (Fig. 1a). By using this one-pot thermal polycondensation process,

a large-scale and rapid synthesis of high-quality HER photocatalysts of graphitic carbon nitride with a high yield of 55 wt.% has been achieved at 550 °C for 30 min, and the photocatalysts consist of unique isotype heterojunctions of triazine-/heptazine based g-C<sub>3</sub>N<sub>4</sub> nanocrystals. For purposes of comparison, the conventional thermal polymerization methods, including electric-resistance heating (er), microwave heating (mw), and electric-resistance molten-salt (er-ms) process, are also used to synthesize g-C<sub>3</sub>N<sub>4</sub> based photocatalysts (Fig. 1a). The photocatalytic HER activity of the isotype triazine-/heptazine based g-C<sub>3</sub>N<sub>4</sub> heterojunctions is much higher than that of the g-C<sub>3</sub>N<sub>4</sub> samples obtained by the above conventional thermal polymerization processes. The phases, chemical compositions, microstructures, optical properties and photocatalytic HER performance of the as-obtained samples are comparatively investigated, and the related mechanisms are analyzed.

## 2. Experimental section

### 2.1. Materials and setup

Melamine (chemically pure, Sinopharm Chemical Reagent Co. Ltd.), LiCl (analytically pure, Sigma-Aldrich), KCl (analytical pure, Tianjin Kermel Chemical Reagent Co. Ltd), triethanolamine (TEOA, analytically pure, Tianjin Fengchuan Chemical Reagent Co., Ltd), H<sub>2</sub>PtCl<sub>6</sub>·6H<sub>2</sub>O (Shanghai Chemical Reagent Co., Ltd), and rhodamine B (RhB, analytically pure, Tianjin Kaitong Chemical Reagent Co., Ltd) were used as received. A commercially available microwave workstation (Mobilelab, Tangshan Nanosource Microwave Thermal Instrument Manufacturing Co. Ltd, Fig. 1b–c), and a conventional electric-resistance furnace (Fig. 1d, heating chamber dimensions: 100 × 100 × 120 mm) were used in the synthesis of g-C<sub>3</sub>N<sub>4</sub> samples.

### 2.2. Materials synthesis

As Fig. 1 shows, four processes were comparatively used to synthesize g-C<sub>3</sub>N<sub>4</sub> photocatalysts.

(1) *Microwave-assisted molten-salt process (mw-ms-g-C<sub>3</sub>N<sub>4</sub>)*. The eutectic mixture of KCl/LiCl (49.4:50.6 in molar ratio) with a melting point about 450 °C was used as the molten salt. Typically, 1.26 g of melamine and 3 g of the above eutectic mixture of KCl/LiCl were fully mixed by grinding them in an agate mortar for more than 5 min. The as-obtained mixture containing melamine (~30 wt.%) and the eutectic salt (70 wt.%) was transferred into a ceramic crucible (20 mL in volume) with a ceramic lid. The above crucible was placed in the center of the microwave heating chamber (Fig. 1b), and then heated to 550 °C with a heating rate of 10 °C min<sup>-1</sup>. The heating treatment was kept at 550 °C for 30 min, and then the sample was naturally cooled down to room temperature. The solid obtained was ground to micro-powders and washed with hot water (200 mL at ~80 °C, stirring for 1 h) to remove KCl/LiCl species. After filtration and washing for 4 times, the solid obtained was dried at 80 °C for more than 12 h. The as-obtained sample was marked as mw-ms-g-C<sub>3</sub>N<sub>4</sub>. For the sake of comparison, some g-C<sub>3</sub>N<sub>4</sub> samples were also synthesized using eutectic KCl/LiCl mixtures with various melting points, e.g., 353 °C (KCl/LiCl = 40.8:59.2) and 400 °C (KCl/LiCl = 45:55), as the polymerization reaction media of melamine via the similar microwave-assisted molten-salt process, and the corresponding samples obtained were marked as mw-ms-353 °C-g-C<sub>3</sub>N<sub>4</sub> and mw-ms-400 °C-g-C<sub>3</sub>N<sub>4</sub>, respectively. Effects of the factors influencing the polymerization reaction, e.g., reaction temperatures (520 °C, 550 °C, 580 °C)

and reaxtion times (15 min, 30 min, 45 min), were investigated using the eutectic KCl/LiCl mixture with a melting point of 450 °C as the reaction media.

- (2) *Electric-resistance molten-salt process (er-ms-g-C<sub>3</sub>N<sub>4</sub>)*. Typically, 1 g of melamine and 5 g of eutectic mixture of KCl/LiCl (40.8:59.2 in molar ratio) with a melting point of ~353 °C were fully ground in an agate mortar, and the as-obtained powder was then transferred to a ceramic crucible (20 mL), which was placed into the center of heating chamber of a muffle furnace (Fig. 1d). The furnace was heated to 550 °C with a heating rate of 10 °C min<sup>-1</sup> and kept at 550 °C for 4 h. The as-obtained solid was ground and washed with hot water, and dried at 80 °C for more than 12 h, and the as-obtained sample was marked as er-ms-g-C<sub>3</sub>N<sub>4</sub> [44].
- (3) *Electric-resistance heating process (er-g-C<sub>3</sub>N<sub>4</sub>)*. Typically, 10 g of melamine was put in a porcelain crucible (20 mL) covered with a lid, which was placed into the electric-resistance muffle furnace (Fig. 1d). The furnace was heated to 550 °C with heating rate of 5 °C min<sup>-1</sup> and the polymerization reaction was kept at 550 °C for 4 h. The as-obtained sample was marked as er-g-C<sub>3</sub>N<sub>4</sub>.
- (4) *Microwave heating process (mw-g-C<sub>3</sub>N<sub>4</sub>)*. Typically, 10 g of melamine was put in a ceramic crucible (20 mL) covered with a lid. The crucible with melamine was placed into the center of the microwave heating chamber (Fig. 1b) and heated at 550 °C for 30 min with a heating rate of 10 °C min<sup>-1</sup>. The as-obtained was marked as mw-g-C<sub>3</sub>N<sub>4</sub>.

### 2.3. Characterization and analysis

Phase compositions of the graphitic carbon nitrides obtained were determined by X-ray diffraction on a D/max 2500 XRD diffractometer (Rigaku) with a Cu K $\alpha$  radiation ( $\lambda = 1.5406 \text{ \AA}$ ) operated at 40 kV and 30 mA, with a scanning rate of 4° min<sup>-1</sup> in  $2\theta = 10\text{--}60^\circ$ . Fourier transform infrared spectra (FT-IR) were recorded on a FT-IR spectrometer (Thermo Fisher Nicloet i50) in the range of 4000–500 cm<sup>-1</sup> at a resolution of 4 cm<sup>-1</sup> using the KBr technique. Raman spectra were obtained using a Raman spectrometer (LabRAM HR Evolution, HORIBA JobinYvon, France) at room temperature using the 633 nm line as the excitation source. The powder samples were fixed on the surface of a SiO<sub>2</sub>/Si substrate. The morphology was observed by scanning electron microscopy (JSM-7001F JEOL, Japan) and transmission electron microscopy (Tecnai F-20-S-TWIN, FEI, America). The UV-vis diffuse reflectance (DR) spectra were conducted on a UV-vis-NIR spectrophotometer (Shimadzu UV-3600) in a wavelength range of 200–800 nm. The photoluminescence (PL) spectra were identified on a spectrofluorometer (FluoroMax-4, HORIBA JobinYvon, France) at a 388 nm line laser at room temperature; the emission spectra ( $\lambda_{\text{em}}$ ) ranged in 400–700 nm (with a 400 nm filter) and both of slits were 2 nm. The time-resolved transient PL (TR-PL) spectra were determined by using a spectrofluorometer (Fluorolog®-3 TCSPC, HORIBA, France) excited by 370 nm laser with emission at 460 nm. X-ray photoelectron spectroscopy (XPS) spectra were performed on an XPS spectroscope (Escalab 250xi, Thermo Scientific Ltd., England) equipped with an Al K $\alpha$  (1486.6 eV) radiation source. The specific surface areas were measured by Brunauer-Emmet-Teller (BET) method on the basis of N<sub>2</sub> adsorption-desorption isotherms obtained on ASAP 2460 (Micromeritics) machine at a liquid nitrogen temperature (~196 °C). Elemental analysis of CHN was measured by a CHNS/O analyzer (Flash EA 112 series Thermo Scientific).

#### 2.4. Photoelectrochemical test

The working electrodes (i.e., photoanodes) were prepared as follows: 5 mg of the g-C<sub>3</sub>N<sub>4</sub> sample was dispersed in 250 μL of dimethyl formamide (DMF) by ultrasonication for 30 min to make a uniform g-C<sub>3</sub>N<sub>4</sub> slurry, which was then coated onto the surface of an FTO glass plate (2.5 × 2.4 cm). Before use, the FTO glass plate was carefully washed with water, ethanol and acetone for 30 min sequentially, and the g-C<sub>3</sub>N<sub>4</sub>/FTO electrodes were dried in air for one day. Photoelectrochemical test was carried out in a standard three-electrode setup on an electrochemical workstation (AMETEK, PARSTAT 4000, America). The electrodes of the Pt wire and Ag/AgCl (saturated KCl) were used as the counter and reference electrode, respectively. The Na<sub>2</sub>SO<sub>4</sub> aqueous solution (0.2 M) was used as the electrolyte. A 300 W Xenon lamp (Beijing Perfectlight Co., Ltd) equipped with a cutoff filter ( $\lambda \geq 420$  nm) was used as the light source. The photocurrent response spectroscopy was measured at a constant potential of +0.9 V vs. the working photoanode. The electrochemical impedance spectroscopy (EIS) was determined at an open-circuit voltage in a frequency range of 10 mHz–100 kHz with an amplitude of 5 mV. The Mott-Schottky plots were recorded on the electrochemical workstation (CHI660E Instruments) using a standard three-electrode system, with a working electrode of photoanodes, a reference electrode of Ag/AgCl and a counter electrode of Pt foil, in an electrolyte of 0.5 M Na<sub>2</sub>SO<sub>4</sub> aqueous solution. The tests were carried on at a frequency of 1 kHz in a potential range of –1.5 to –1 V (vs. Ag/AgCl) under dark condition.

#### 2.5. Test of photocatalytic hydrogen evolution

The test of photocatalytic hydrogen evolution reaction (HER) activity of the g-C<sub>3</sub>N<sub>4</sub> samples was carried out in a commercially available HER system (CEL-SPH2N, Beijing China Education Au-light Co., Ltd., China). Typically, 50 mg of the g-C<sub>3</sub>N<sub>4</sub> photocatalyst and 0.3 mL of H<sub>2</sub>PtCl<sub>6</sub>·6H<sub>2</sub>O aqueous solution (0.0256 mol L<sup>−1</sup>) were added in a Pyrex top-irradiation reaction vessel and then dispersed in 50 mL of triethanolamine aqueous solution (TEOA, 10 vol.%) by ultrasonication for 10 min. Then a co-catalyst of 3 wt% Pt was photo-deposited on the surfaces of the g-C<sub>3</sub>N<sub>4</sub> samples by UV-vis irradiation (CEL-XHF 300, Beijing China Education Au-light Co., Ltd., China) for 1 h. The Pyrex reaction vessel with the g-C<sub>3</sub>N<sub>4</sub> based photocatalyst was carefully fixed and sealed to the photocatalytic HER system, of which the air impermeability was carefully checked by being vacuumed and kept for more than 30 min. During the photocatalytic HER test, a 300 W Xenon lamp equipped with a 420 nm cut-off filter was used as the irradiation source. The amount of hydrogen generated was analyzed by a gas chromatographer (GC 7920, Beijing China Education Au-light Co., Ltd., China) using high-purity N<sub>2</sub> (99.999%) as the carrier gas.

The apparent quantum yield (AQY) of the g-C<sub>3</sub>N<sub>4</sub> sample was measured by using a Xe lamp with a monochromatic light filter of 420 nm. The AQY was calculated as the follow equation (Eq. (1)) [60]:

$$AQY = \frac{N_e}{N_p} \times 100\% = \frac{2MN_Ahc}{SPt\lambda} \times 100\% \quad (1)$$

where,  $N_e$  and  $N_p$  mean the amounts of reaction electrons and incident photons, respectively;  $M$  is the amount of hydrogen molecules, and  $N_A$ ,  $h$  and  $c$  are Avogadro's constant, Planck constant and the speed of light, respectively;  $S$  is the irradiation area,  $P$  is the intensity of irradiation,  $t$  means the photoreaction time, and  $\lambda$  is the wavelength of incident light ( $\lambda = 420$  nm).

#### 2.6. Test of photocatalytic degradation activity of rhodamine B

Photocatalytic degradation of rhodamine B (RhB) with the obtained g-C<sub>3</sub>N<sub>4</sub> samples was conducted under a visible-light ( $\lambda \geq 420$  nm) irradiation using a 300 W Xe lamp (NBeT, HSX-F300) equipped with an ultraviolet cutoff filter (420 nm). The light density used was about 200 mw cm<sup>−2</sup>. Typically, 50 mg of g-C<sub>3</sub>N<sub>4</sub> sample was dispersed in a 50 mL aqueous solution of RhB (10 mg L<sup>−1</sup>) (i.e., sonication for 5 min) under a dark condition by rigorously covering the above solution using an aluminum foil. Before visible-light irradiation, the above suspension was kept magnetically stirring in dark for 30 min to reach a dye-absorption equilibrium on the g-C<sub>3</sub>N<sub>4</sub> photocatalysts. During the test of photocatalytic degradation, 5 mL of the suspensions were drawn from the reaction system every 10 min. The as-obtained suspensions drawn out were centrifuged at 5000 rpm for 5 min twice to remove the solid photocatalyst particles, and the upper clear solutions were then transferred to a quartz cuvette (1 × 1 cm) to measure their absorption spectra using a UV-vis spectrophotometer (UV-1800PC, Mapada Instruments, China). According to the Lambert-Beer law ( $A = \lg(1/T) = kC$ ), the RhB concentrations ( $C$ ) of the solutions are in direct proportion to their absorbance ( $A$ ) at 551 nm.

### 3. Results and discussion

#### 3.1. Synthesis, photocatalytic and photoelectrochemical properties

The graphitic carbon nitride (g-C<sub>3</sub>N<sub>4</sub>) sample of mw-ms-g-C<sub>3</sub>N<sub>4</sub> was firstly synthesized using the microwave-assisted molten-salt (mw-ms) process (Fig. 1) at 550 °C for 30 min with melamine as the single-source precursor. For the sake of comparisons, three typical g-C<sub>3</sub>N<sub>4</sub> samples were synthesized by electric-resistance molten-salt process (er-ms-g-C<sub>3</sub>N<sub>4</sub>), electric-resistance heating process (er-g-C<sub>3</sub>N<sub>4</sub>) [8,44], and microwave heating process (mw-g-C<sub>3</sub>N<sub>4</sub>). Fig. 1e and f compare the reaction times and typical yields of g-C<sub>3</sub>N<sub>4</sub> in the various synthetic processes. When compared with the er process (51–61%, 240 min) and the mw one (44%, 30 min), the mw-ms process gives a higher yield of 55% in a shorter reaction time of 30 min.

Firstly, the HER activity of the g-C<sub>3</sub>N<sub>4</sub> samples was comparatively evaluated. Fig. 2a shows the typical curves of the amount of H<sub>2</sub> generated as a function of irradiation time in the presence of g-C<sub>3</sub>N<sub>4</sub> samples loading ~3 wt.% Pt in 10 vol.% TEOA aqueous solution upon exposure to visible-light irradiation ( $\lambda \geq 420$  nm). The hydrogen amounts generated increase linearly with the irradiation times for the four samples. After reaction for 4 h, the cumulative hydrogen amount of mw-ms-g-C<sub>3</sub>N<sub>4</sub> is up to 304 μmol, whereas the cumulative hydrogen amounts of the samples of er-ms-g-C<sub>3</sub>N<sub>4</sub>, er-g-C<sub>3</sub>N<sub>4</sub>, and mw-g-C<sub>3</sub>N<sub>4</sub> are 60, 19 and 13 μmol, respectively. Fig. 2b compares the HER rates of the g-C<sub>3</sub>N<sub>4</sub> samples. The HER rate of mw-ms-g-C<sub>3</sub>N<sub>4</sub> is about 1480 μmol g<sup>−1</sup> h<sup>−1</sup>, which is 5 times that (300 μmol g<sup>−1</sup> h<sup>−1</sup>) of er-ms-g-C<sub>3</sub>N<sub>4</sub>, and 15 times that (95 μmol g<sup>−1</sup> h<sup>−1</sup>) of er-g-C<sub>3</sub>N<sub>4</sub> and 23 times that (63 μmol g<sup>−1</sup> h<sup>−1</sup>) of mw-g-C<sub>3</sub>N<sub>4</sub>. It is worth noting that the g-C<sub>3</sub>N<sub>4</sub> sample obtained by the mw-ms process has the highest HER activity under the visible-light condition among the four samples. In addition, the apparent quantum yield (AQY) of the mw-ms-g-C<sub>3</sub>N<sub>4</sub> sample was measured at an incident light wavelength of  $\lambda = 420$ , and its typical AQY is as high as 10.7%, which is competitive in the existing literature reports of g-C<sub>3</sub>N<sub>4</sub> photocatalysts for HER applications [44,64–66].

The photocurrents and electrochemical impedance spectroscopies of the g-C<sub>3</sub>N<sub>4</sub> samples obtained via various processes were investigated for furthermore understanding their photoelectric

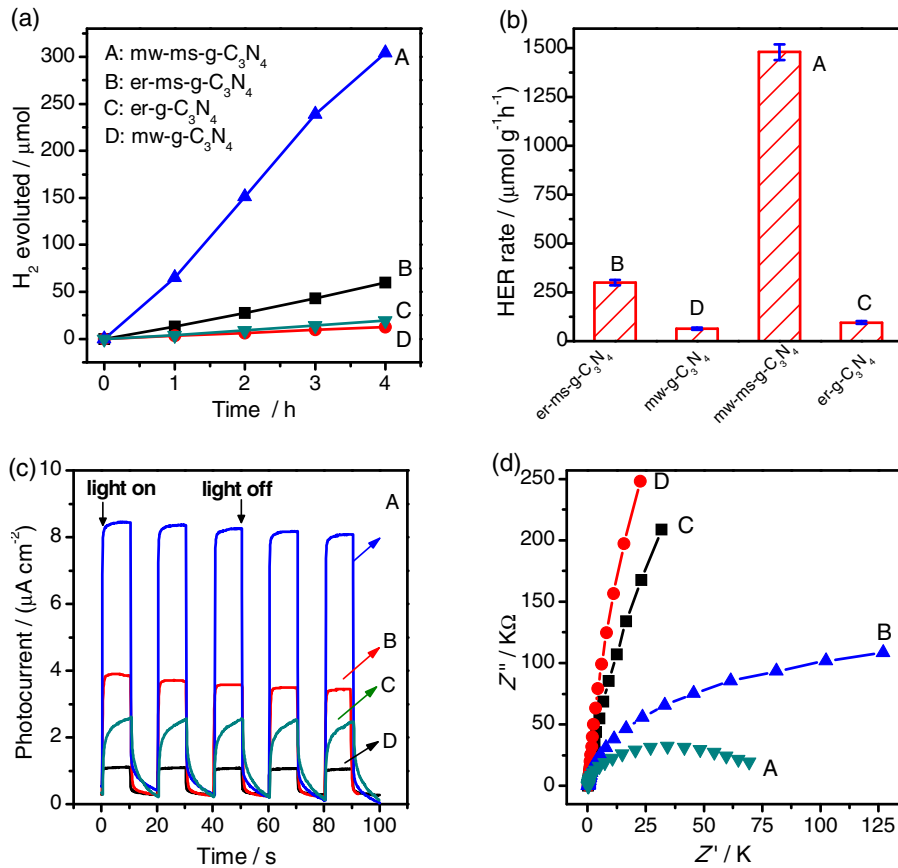


**Fig. 2.** (a) Amounts of photocatalytic hydrogen evolution as a function of reaction time under visible light irradiation ( $\lambda \geq 420$  nm) in the presence of  $\text{g-C}_3\text{N}_4$  samples obtained by different processes; (b) Comparison of the rates of photocatalytic  $\text{H}_2$  evolution; (c) Transient photocurrents recorded under visible light irradiation ( $\lambda \geq 420$  nm); (d) The EIS Nyquist plots of the 4 samples: (A) mw-ms-g-C<sub>3</sub>N<sub>4</sub>, (B) er-ms-g-C<sub>3</sub>N<sub>4</sub>, (C) er-g-C<sub>3</sub>N<sub>4</sub>, and (D) mw-g-C<sub>3</sub>N<sub>4</sub>.

performance. Fig. 2c shows the transient photocurrent vs. irradiation time recorded under visible light irradiation ( $\lambda \geq 420$  nm). The mw-ms-g-C<sub>3</sub>N<sub>4</sub> sample (A) shows a significantly enhanced photocurrent upon exposure to visible light irradiation compared with the other g-C<sub>3</sub>N<sub>4</sub> samples (B-D). Also, the g-C<sub>3</sub>N<sub>4</sub> samples (A and B) obtained by the molten-salt process show higher photocurrent responses than those (C and D) obtained direct thermo-polymerization. The transient photocurrent response is a qualitative approach to investigate the separation efficiency of photo-generated electron-hole pairs [45]. The highest photocurrent for the mw-ms-g-C<sub>3</sub>N<sub>4</sub> sample indicates that this sample is of the highest efficiency in separation of photo-generated electron-hole pairs. Electrochemical impedance spectroscopy (EIS) is an intuitive approach to determine the electron transfer efficiency. Fig. 2d shows the EIS Nyquist plots of the g-C<sub>3</sub>N<sub>4</sub> samples obtained. The arc radius of the semicircular Nyquist plot for the mw-ms-g-C<sub>3</sub>N<sub>4</sub> sample (A) obtained by microwave-assisted molten-salt process is much smaller than that of the other g-C<sub>3</sub>N<sub>4</sub> samples (B-D), suggesting that the mw-ms-g-C<sub>3</sub>N<sub>4</sub> sample has the smallest electron-transfer resistance and the highest electrical conductivity. The EIS result highly agrees with the photocurrent response and photocatalytic HER performance of the g-C<sub>3</sub>N<sub>4</sub> samples obtained via various processes.

### 3.2. Phase composition, morphology and microstructure

To understand their photocatalytic HER behavior, we carefully characterized the phase compositions, morphologies and microstructures of the g-C<sub>3</sub>N<sub>4</sub> samples using the typical techniques of X-ray diffraction (XRD), elemental analysis (EA), Fourier trans-

form infrared (FT-IR) spectroscopy, SEM, N<sub>2</sub> adsorption-desorption isotherms, TEM and X-ray photoelectron spectroscopy (XPS).

The phases of the g-C<sub>3</sub>N<sub>4</sub> samples were determined by the XRD analysis, and Fig. 3a shows their typical XRD patterns. The samples of mw-g-C<sub>3</sub>N<sub>4</sub> (D) and er-g-C<sub>3</sub>N<sub>4</sub> (C) show two diffraction peaks at  $2\theta = 13.0^\circ$  and  $27.4^\circ$ . The strong peaks at  $27.4^\circ$ , due to the stacking of conjugated aromatic rings in the discotic systems, can be assignable to the (002) plane of the typical g-C<sub>3</sub>N<sub>4</sub> phase (i.e., heptazine-based g-C<sub>3</sub>N<sub>4</sub>), and the weak one locates at  $2\theta = 13.0^\circ$  can be recognized as the (100) plane, corresponding to the in-plane arrangement of nitrogen-linked heterocyclic rings [8]. The XRD pattern (B) of er-ms-g-C<sub>3</sub>N<sub>4</sub> shows a series of peaks at  $12.0^\circ$ ,  $21^\circ$ ,  $24.3^\circ$ ,  $26.4^\circ$ ,  $29.1^\circ$  and  $32.4^\circ$ , which can be indexed to the deflections from the (100), (110), (200), (002), (102) and (210) planes of the poly(triazine imide) (PTI) phase (i.e., triazine-based g-C<sub>3</sub>N<sub>4</sub>), and the (100) and (002) diffraction planes correspond to the in-plane arrangement of nitrogen-linked heterocyclic rings and the stacking of the conjugated aromatic rings, respectively [31]. Comparatively, the XRD pattern of the mw-ms-g-C<sub>3</sub>N<sub>4</sub> sample (A) seems to be a superimposition of pattern B and C. The peaks at  $12.0^\circ$ ,  $21^\circ$ ,  $24.3^\circ$ ,  $26.4^\circ$ ,  $29.1^\circ$  and  $32.4^\circ$  can be indexed to the triazine-based g-C<sub>3</sub>N<sub>4</sub> phase, whereas the peak at  $\sim 27.8^\circ$  can be indexed to the (002) plane of the heptazine-based g-C<sub>3</sub>N<sub>4</sub> phase. When compared with er-g-C<sub>3</sub>N<sub>4</sub> and mw-g-C<sub>3</sub>N<sub>4</sub>, the diffraction peak from the (002) plane of the mw-ms-g-C<sub>3</sub>N<sub>4</sub> sample moves from  $27.4^\circ$  to  $27.8^\circ$ , which suggests that the mw-ms-g-C<sub>3</sub>N<sub>4</sub> sample is of a decreased interlayer distance [46,47]. According to the XRD results, the samples of mw-g-C<sub>3</sub>N<sub>4</sub> (D) and er-g-C<sub>3</sub>N<sub>4</sub> (C) have a heptazine-based g-C<sub>3</sub>N<sub>4</sub> phase, and the er-ms-g-C<sub>3</sub>N<sub>4</sub> sample consists of a triazine-based g-C<sub>3</sub>N<sub>4</sub>

**Table 1**Summary of elemental analysis, hydrogen evolution rate and yields of the g-C<sub>3</sub>N<sub>4</sub> samples.

Sample	C (wt.%)	N (wt.%)	H (wt.%)	Apparent formula	Atomic C/N ratio	H <sub>2</sub> rate (μmol g <sup>-1</sup> h <sup>-1</sup> )	Reaction temperature and period	Yield (wt.%)
mw-ms-g-C <sub>3</sub> N <sub>4</sub>	28.4	45.7	2.4	C <sub>3.0</sub> N <sub>4.1</sub> H <sub>3.0</sub>	0.73	1480	550 °C/30 min	55
er-ms-g-C <sub>3</sub> N <sub>4</sub>	24.4	40.2	2.3	C <sub>3.0</sub> N <sub>4.2</sub> H <sub>3.4</sub>	0.71	300	550 °C/240 min	51
er-g-C <sub>3</sub> N <sub>4</sub>	34.7	62.6	1.7	C <sub>3.0</sub> N <sub>4.6</sub> H <sub>1.7</sub>	0.65	93	550 °C/240 min	61
mw-g-C <sub>3</sub> N <sub>4</sub>	34.6	61.1	1.9	C <sub>3.0</sub> N <sub>4.5</sub> H <sub>2.0</sub>	0.67	65	550 °C/30 min	44

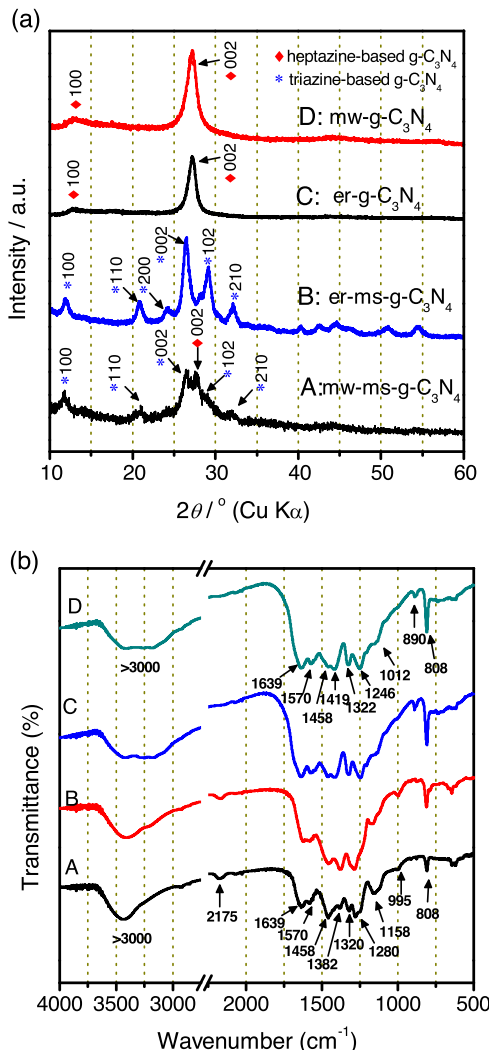


Fig. 3. (a) Typical XRD patterns (b) FT-IR spectra of the g-C<sub>3</sub>N<sub>4</sub> photocatalysts obtained via different processes: (A) mw-ms-g-C<sub>3</sub>N<sub>4</sub>, (B) er-ms-g-C<sub>3</sub>N<sub>4</sub>, (C) er-g-C<sub>3</sub>N<sub>4</sub>, and (D) mw-g-C<sub>3</sub>N<sub>4</sub>.

phase; while the mw-ms-g-C<sub>3</sub>N<sub>4</sub> sample is composed of the hybrid of triazine-based g-C<sub>3</sub>N<sub>4</sub> and heptazine-based g-C<sub>3</sub>N<sub>4</sub> phases.

The elemental analysis (EA) data (e.g., CHN results) of the as-obtained g-C<sub>3</sub>N<sub>4</sub> samples are listed in Table 1. Calculated according to the CHN results, the apparent formula of mw-ms-g-C<sub>3</sub>N<sub>4</sub>, er-ms-g-C<sub>3</sub>N<sub>4</sub>, er-g-C<sub>3</sub>N<sub>4</sub> and mw-g-C<sub>3</sub>N<sub>4</sub> can be C<sub>3.0</sub>N<sub>4.1</sub>H<sub>3.0</sub>, C<sub>3.0</sub>N<sub>4.2</sub>H<sub>3.4</sub>, C<sub>3.0</sub>N<sub>4.6</sub>H<sub>1.7</sub> and C<sub>3.0</sub>N<sub>4.5</sub>H<sub>2.0</sub>, respectively. The EA results of er-g-C<sub>3</sub>N<sub>4</sub> and mw-g-C<sub>3</sub>N<sub>4</sub> are similar to the literature data [44]. The elemental compositions of mw-ms-g-C<sub>3</sub>N<sub>4</sub> and er-ms-g-C<sub>3</sub>N<sub>4</sub> are similar, but the atomic C/N ratio of mw-ms-g-C<sub>3</sub>N<sub>4</sub> is slightly larger than that of er-ms-g-C<sub>3</sub>N<sub>4</sub>. This result suggests that the microwave-assisted molten-salt process favors in forming more N vacancies [48].

The chemical compositions of the g-C<sub>3</sub>N<sub>4</sub> samples are further determined by FT-IR spectra, shown as Fig. 3b. One can see that the

FT-IR spectrum of mw-ms-g-C<sub>3</sub>N<sub>4</sub> is similar to that of er-ms-g-C<sub>3</sub>N<sub>4</sub> (spectra A, B in Fig. 3b), and that the FT-IR spectra of er-g-C<sub>3</sub>N<sub>4</sub> and mw-g-C<sub>3</sub>N<sub>4</sub> are similar (spectra C, D in Fig. 3b). The similarity in FT-IR spectra agrees with their XRD results (Fig. 3a). For the samples of er-g-C<sub>3</sub>N<sub>4</sub> (C) and mw-g-C<sub>3</sub>N<sub>4</sub> (D), the strong bands at 808 cm<sup>-1</sup> are assignable to the breathing mode of triazine-based units, and the peaks in the region of 1000–1700 cm<sup>-1</sup> can be attributed to the stretching mode of CN heterocycles [30]. The peaks at 1246, 1322 and 1419 cm<sup>-1</sup> correspond to the vibrations of aromatic N–C groups, and the peaks at 1570 and 1639 cm<sup>-1</sup> are due to the C=N vibrations. The bands in the region of >3000 cm<sup>-1</sup> can be assigned to secondary and primary amines and their intermolecular hydrogen bonding [30,48,49]. From the FT-IR spectrum (A) of mw-ms-g-C<sub>3</sub>N<sub>4</sub>, similar to that (B) of er-ms-g-C<sub>3</sub>N<sub>4</sub>, one can find that the intensity of the broad band at 3250 cm<sup>-1</sup> is weaker than that of the spectra C and D, suggesting that the amount of –NH groups in mw-ms-g-C<sub>3</sub>N<sub>4</sub> and er-ms-g-C<sub>3</sub>N<sub>4</sub> is less than that of er-g-C<sub>3</sub>N<sub>4</sub> and mw-g-C<sub>3</sub>N<sub>4</sub> [8]. The distinct bands at ~2175 cm<sup>-1</sup> in mw-ms-g-C<sub>3</sub>N<sub>4</sub> and er-ms-g-C<sub>3</sub>N<sub>4</sub> (A, B) indicate the presence of terminal cyano groups [33]. Some characteristic peaks in the FT-IR spectra, e.g., the peaks at 890 cm<sup>-1</sup> in er-g-C<sub>3</sub>N<sub>4</sub> and mw-g-C<sub>3</sub>N<sub>4</sub> and the peaks at 995, 2175 cm<sup>-1</sup> in mw-ms-g-C<sub>3</sub>N<sub>4</sub> and er-ms-g-C<sub>3</sub>N<sub>4</sub>, can corroborate the difference in surface chemical compositions, although they are difficult to be indexed to any specific species. Raman spectra were also used to characterize these g-C<sub>3</sub>N<sub>4</sub> samples (Fig. S2, ESI†), but no obvious peaks can be found in their Raman spectra.

The morphologies of the g-C<sub>3</sub>N<sub>4</sub> samples were observed comparatively by SEM, and Fig. 4 shows their typical SEM images. According to the SEM images, all the samples seem to consist of large particulate bulks, which are composed of various sub-particles. For mw-ms-g-C<sub>3</sub>N<sub>4</sub> (Fig. 4a), the bulks seem to be loose aggregates of nanoplates [50]. Comparatively, the er-ms-g-C<sub>3</sub>N<sub>4</sub> sample (Fig. 4b) consists of rod-like particles, which are the assembly of smaller g-C<sub>3</sub>N<sub>4</sub> nanorods (~100 nm in diameter); the samples of er-g-C<sub>3</sub>N<sub>4</sub> (Fig. 4c) and mw-g-C<sub>3</sub>N<sub>4</sub> (Fig. 4d) consist of large and compact g-C<sub>3</sub>N<sub>4</sub> particles.

The specific surface areas and microstructures of the g-C<sub>3</sub>N<sub>4</sub> samples obtained via different processes were characterized using N<sub>2</sub> adsorption-desorption isotherms. Fig. 5 shows their typical N<sub>2</sub> adsorption-desorption isotherms, which show a similar shape of type IV for all samples. The specific surface areas calculated by the BET method ( $S_{BET}$ ) are 25.7, 58.1, 10.6, and 7.1 m<sup>2</sup> g<sup>-1</sup>, for mw-ms-g-C<sub>3</sub>N<sub>4</sub> (A), er-ms-g-C<sub>3</sub>N<sub>4</sub> (B), er-g-C<sub>3</sub>N<sub>4</sub> (C) and mw-g-C<sub>3</sub>N<sub>4</sub> (D), respectively. Taking their SEM images (Fig. 4) into account, the samples of mw-ms-g-C<sub>3</sub>N<sub>4</sub> and er-ms-g-C<sub>3</sub>N<sub>4</sub> have larger  $S_{BET}$  values than those of er-g-C<sub>3</sub>N<sub>4</sub> and mw-g-C<sub>3</sub>N<sub>4</sub> (D), indicating that molten-salt media are helpful to synthesize g-C<sub>3</sub>N<sub>4</sub> with higher specific surface areas. It is worth noting that the HER activity of the mw-ms-g-C<sub>3</sub>N<sub>4</sub> sample is much higher than that of the er-ms-g-C<sub>3</sub>N<sub>4</sub> sample, although the  $S_{BET}$  of mw-ms-g-C<sub>3</sub>N<sub>4</sub> is smaller than that of er-ms-g-C<sub>3</sub>N<sub>4</sub>. Therefore, the specific surface area is not the essential factor determining the photocatalytic performance of the g-C<sub>3</sub>N<sub>4</sub> samples. Also, among the four g-C<sub>3</sub>N<sub>4</sub> samples, mw-ms-g-C<sub>3</sub>N<sub>4</sub> shows the best dispersibility in water (Fig. S3, ESI†). The higher dispersibility can achieve more uniformly, sufficient photo-deposition of Pt co-catalyst [51], and then be helpful to achieve a higher photocatalytic HER activity.

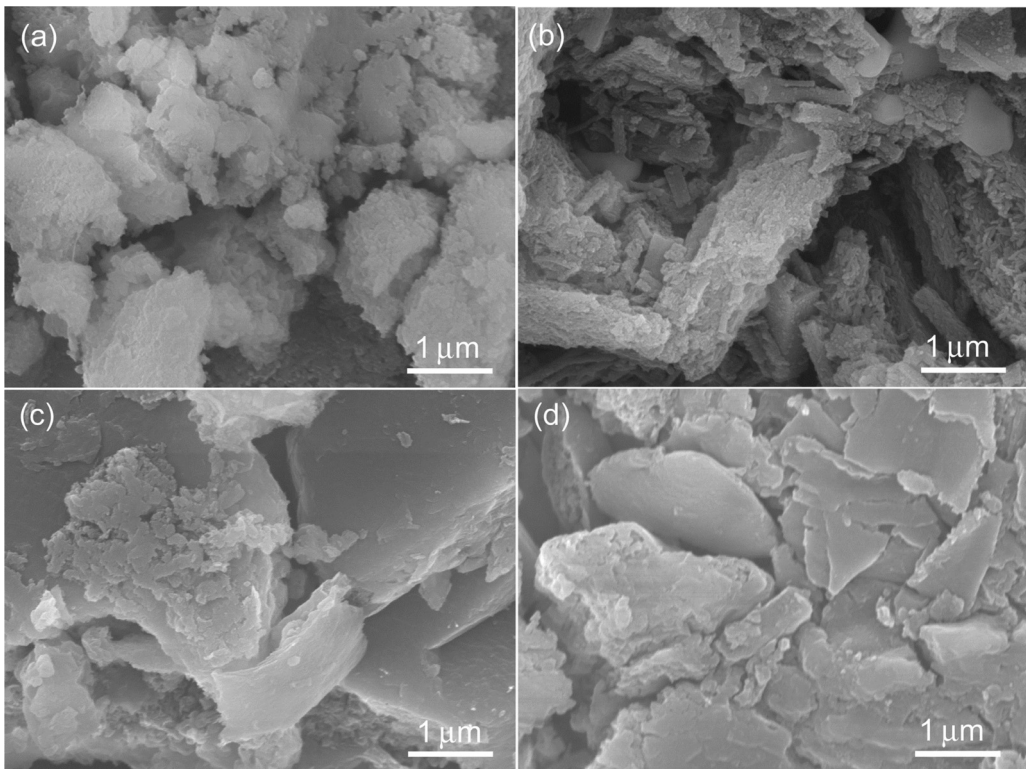


**Fig. 4.** Typical SEM images of the as-obtained  $\text{g-C}_3\text{N}_4$  samples: (a) mw-ms-g- $\text{C}_3\text{N}_4$ , (b) er-ms-g- $\text{C}_3\text{N}_4$ , (c) er-g- $\text{C}_3\text{N}_4$ , and (d) mw-g- $\text{C}_3\text{N}_4$ .

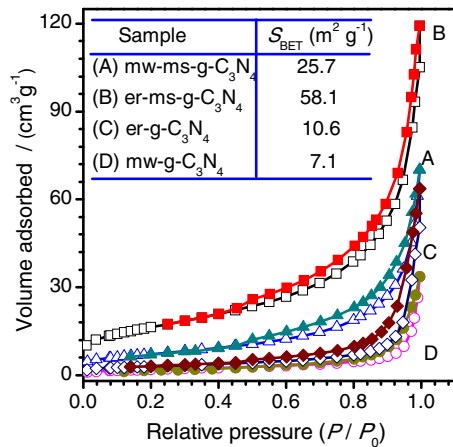


**Fig. 5.** Nitrogen adsorption-desorption isotherms of the as-obtained  $\text{g-C}_3\text{N}_4$  samples: (A) mw-ms-g- $\text{C}_3\text{N}_4$ , (B) er-ms-g- $\text{C}_3\text{N}_4$ , (C) er-g- $\text{C}_3\text{N}_4$ , and (D) mw-g- $\text{C}_3\text{N}_4$ .

For further understanding the microstructures, we observed the typical  $\text{g-C}_3\text{N}_4$  samples of mw-ms-g- $\text{C}_3\text{N}_4$  and er-ms-g- $\text{C}_3\text{N}_4$  using a TEM microscope (Fig. 6). Fig. 6a–e shows the TEM images of mw-ms-g- $\text{C}_3\text{N}_4$ . The low-magnification TEM images (Fig. 6a, b) indicate that the mw-ms-g- $\text{C}_3\text{N}_4$  sample consists of thin plate-like particles. The enlarged TEM images (Fig. 6c, d) show that some small fragments are attached on the surfaces of the large plate-like particles. A high-resolution TEM (HR-TEM) image in Fig. 6e shows that most part of the large plate is amorphous, but some islands (e.g., point A) are well crystallized. The diffraction ring and some dots in the selected area electron diffraction (SAED) pattern (inset of Fig. 6e) corroborate the above HRTEM observations. As the HRTEM image of point A (inset of Fig. 6e) shows, the clear spacing of 0.336 nm can be indexed to the (002) facets of polymer triazine imide [30]. Comparatively, the TEM images of er-ms-g- $\text{C}_3\text{N}_4$  are shown in Fig. 6f–i. The

low-magnification TEM images (Fig. 6f, g) suggest that the er-ms-g- $\text{C}_3\text{N}_4$  sample consists of rod-like particles, which are aggregates of smaller  $\text{g-C}_3\text{N}_4$  nanorods. The enlarged TEM image in Fig. 6h indicates that the small  $\text{g-C}_3\text{N}_4$  nanorods with a diameter of  $\sim 25$  nm are crystalline. As Fig. 6i shows, the loose aggregates of  $\text{g-C}_3\text{N}_4$  nanorods form pores, resulting in a larger  $S_{\text{BET}}$  value.

The specific bonding and surface chemical states of the mw-ms-g- $\text{C}_3\text{N}_4$  sample was further characterized using XPS spectra and Fig. 7 shows its typical XPS spectra. The survey scan in Fig. 7a indicates that there are elements of C, N, O, K and Cl in the mw-ms-g- $\text{C}_3\text{N}_4$  sample. Clearly, elemental C and N belong to  $\text{g-C}_3\text{N}_4$ , O may be due to the O-containing species adsorbed, and elemental K and Cl should be the residue of molten salt (KCl) entrapped in the framework of the  $\text{g-C}_3\text{N}_4$  structure. Fig. 7b shows the high-resolution XPS spectrum of C1s, of which there are three peaks at 284.8, 286.5 and 288.3 eV according to the peak fitting result. The peak at 288.3 eV corresponds to C=N=C in the heterocycle rings, the peak at 286.5 eV is due to C=OH, and the peak at 284.8 eV is assignable to C=C in adventitious carbon [8]. Besides, the peaks at 293.0 and 295.8 eV are assignable to K 2p of K<sup>+</sup> [33]. Fig. 7d shows the O1s XPS spectrum, of which the peak at 532.0 eV indicates the existence of N—C—O groups and the one at 533 eV belongs to surface adsorbed water [52]. Fig. 7c shows the XPS spectrum of N1s, which can be subdivided to be four peaks at 398.8, 399.4, 400.7 and 404.2 eV, corresponding to sp<sup>2</sup>-hybridized nitrogen (C=N=C), tertiary nitrogen (NC<sub>3</sub>), amino functional groups (NH<sub>x</sub> groups) and π excitation, respectively [25]. The tertiary nitrogen peak at 399.4 eV confirms the presence of the heptazine heterocyclic structure [25]. According to the XPS spectra, the atomic ratio of NC<sub>3</sub> to C=N=C is 1:8.6, which is less than the theoretical value (1:6) of the pure heptazine ring. What's more, the atomic ratio of ring nitrogen (NC<sub>3</sub> and C=N=C) to amine nitrogen (NH<sub>x</sub>) is 3.3:1, which is less than the theoretical value (7:2) of the heptazine ring but larger than 2:1 of the triazine ring. This result suggests that the mw-ms-g- $\text{C}_3\text{N}_4$  sample probably consists of the hybrid of heptazine ring and tri-

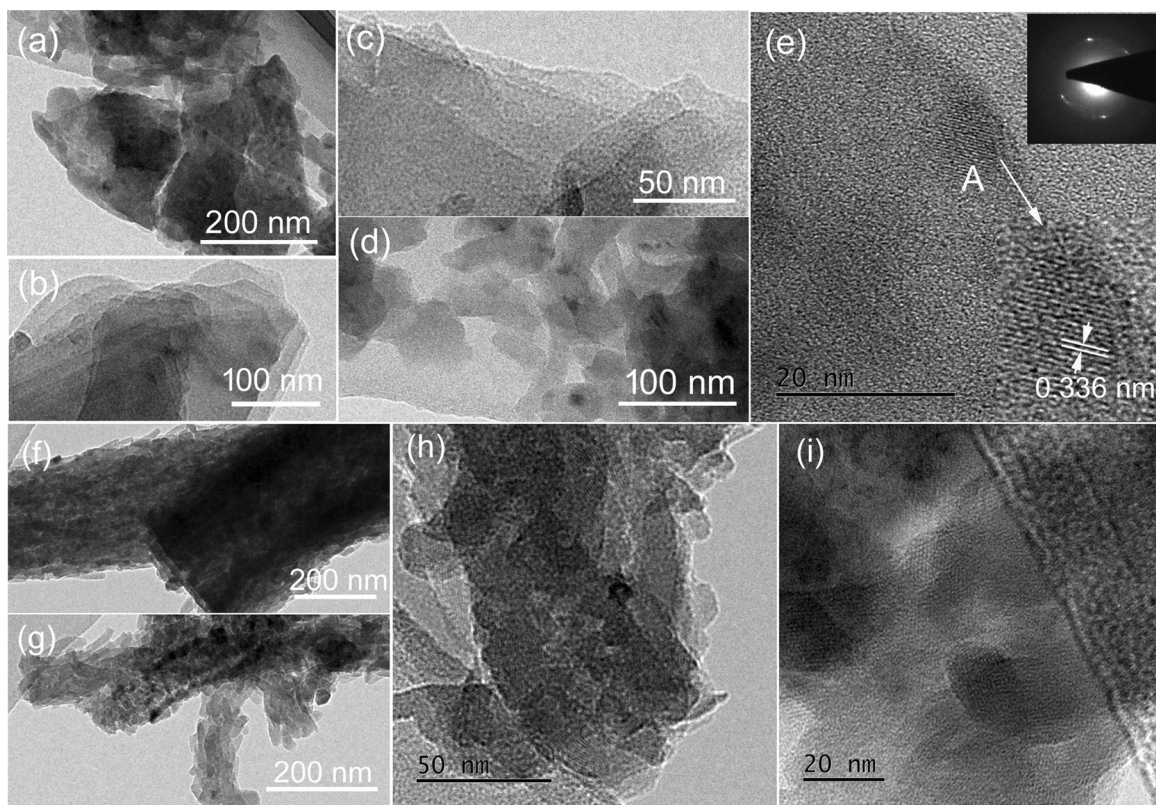


**Fig. 6.** Typical TEM images of the g-C<sub>3</sub>N<sub>4</sub> samples obtained via (a–e) the microwave-assisted molten-salt process (mw-ms-g-C<sub>3</sub>N<sub>4</sub>), and (f–i) the electric-resistance molten-salt process (er-ms-g-C<sub>3</sub>N<sub>4</sub>).

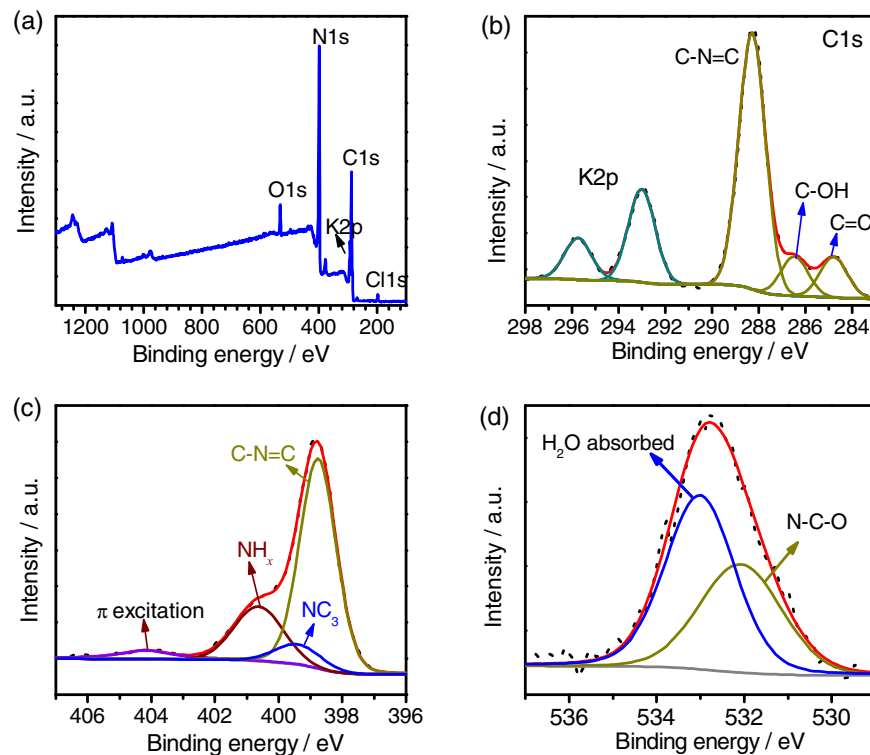


**Fig. 7.** XPS spectra of the g-C<sub>3</sub>N<sub>4</sub> sample (mw-ms-g-C<sub>3</sub>N<sub>4</sub>) obtained via the microwave-assisted molten-salt process: (a) survey scan, (b) C1s, (c) N1s, and (d) O1s.

azine ring. According to the XPS results, the atomic ratio of C/N is 0.72, which is very close to 0.73 calculated by EA analysis in Table 1, suggesting the reliability of the composition analysis. According to

the above XPS analysis and their theoretic structures, the molar ratio of the triazine-based units and heptazine-based units in the mw-ms-g-C<sub>3</sub>N<sub>4</sub> sample is about 13:15, close to 1:1.

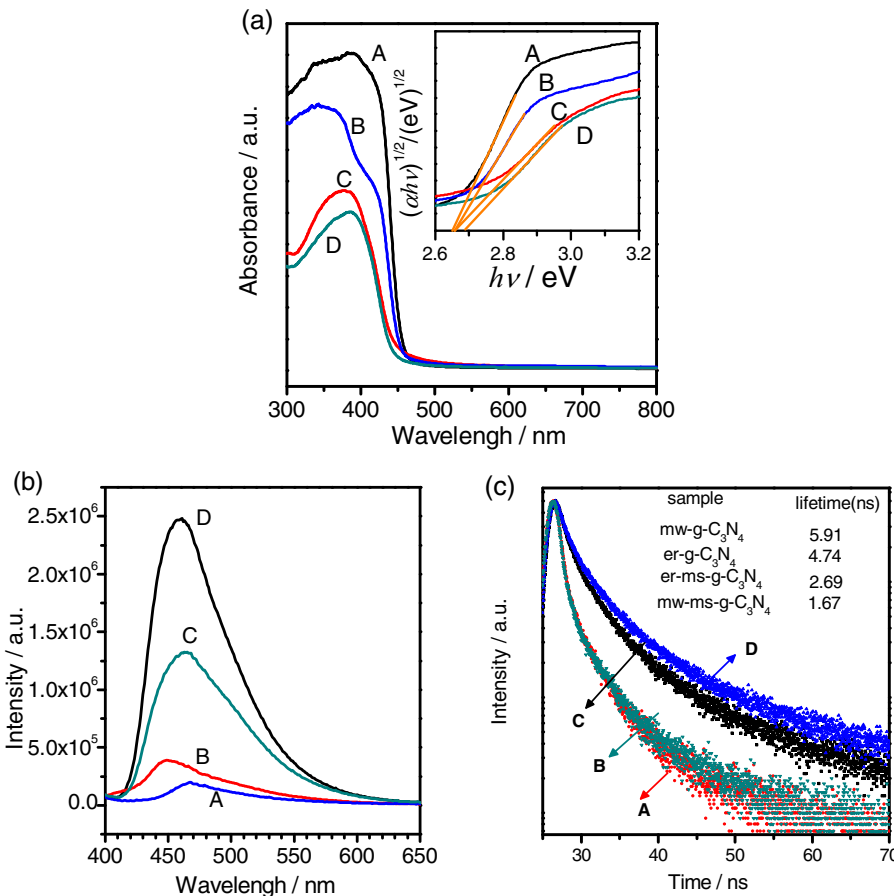


**Fig. 8.** (a) UV-vis absorption spectra converted from reflection to absorbance by the standard Kubelka–Munk method and the corresponding plots of  $(\alpha h\nu)^{1/2}$  vs photon energy ( $h\nu$ ) for the band gap energy of as-obtained g-C<sub>3</sub>N<sub>4</sub> samples; (b) Photoluminescence (PL) spectra of the g-C<sub>3</sub>N<sub>4</sub> samples under 388 nm excitation at room temperature; (c) Time-resolved transient PL decay spectra of the g-C<sub>3</sub>N<sub>4</sub> samples probed at 460 nm (excited by a 370 nm laser): (A) mw-ms-g-C<sub>3</sub>N<sub>4</sub>, (B) er-ms-g-C<sub>3</sub>N<sub>4</sub>, (C) er-g-C<sub>3</sub>N<sub>4</sub>, and (D) mw-g-C<sub>3</sub>N<sub>4</sub>.

Taking the XPS, EA and XRD results into account, we can conclude that the heptazine-based g-C<sub>3</sub>N<sub>4</sub> and triazine-based g-C<sub>3</sub>N<sub>4</sub> are co-existence in the sample of ms-mw-g-C<sub>3</sub>N<sub>4</sub>. The heptazine-based rings and triazine-based rings can be connected one another, and some K<sup>+</sup> ions and other vacancies can be fixed in the rings or between them [53]. The possible formation mechanism will be discussed later. Therefore, the ms-mw-g-C<sub>3</sub>N<sub>4</sub> sample consists of isotype triazine-/heptazine based g-C<sub>3</sub>N<sub>4</sub> heterojunctions, the er-ms-g-C<sub>3</sub>N<sub>4</sub> sample consists of triazine-based g-C<sub>3</sub>N<sub>4</sub> phase (PTI), and the samples of er-g-C<sub>3</sub>N<sub>4</sub> and mw-g-C<sub>3</sub>N<sub>4</sub> are composed of the heptazine based g-C<sub>3</sub>N<sub>4</sub> phase. The difference in phases may account for their difference in photocatalytic HER performance.

### 3.3. Understanding of formation mechanism and enhancement in performance

For further understanding of the electronic band structures and photocatalytic properties, the UV-vis spectra, photoluminescence (PL) spectra and time-resolved transient PL decay (TR-PL) spectra were used to characterize the g-C<sub>3</sub>N<sub>4</sub> samples obtained by various processes.

Fig. 8a shows the UV-vis absorption spectra converted from reflection to absorbance by the standard Kubelka–Munk method. The as-obtained g-C<sub>3</sub>N<sub>4</sub> samples show obvious absorption from UV to ~460 nm, and the characteristic absorption at around 380 nm can be attributed to  $\pi-\pi^*$  electron transition in the conjugated aromatic ring system. In order to calculate the band gaps, the corresponding  $(\alpha h\nu)^{1/2}$  was plotted versus the photon energy ( $h\nu$ ) [51], and the

results are shown in the inset of Fig. 8a. According to the linear-fit lines, the band gaps of mw-ms-g-C<sub>3</sub>N<sub>4</sub> (A), er-ms-g-C<sub>3</sub>N<sub>4</sub> (B), er-g-C<sub>3</sub>N<sub>4</sub> (C) and mw-g-C<sub>3</sub>N<sub>4</sub> (D) are calculated to be  $E_g(A) = 2.65$  eV,  $E_g(B) = 2.66$  eV,  $E_g(C) = 2.66$  eV and  $E_g(D) = 2.70$  eV, respectively, by extrapolating their plots to  $(\alpha h\nu)^{1/2} = 0$ . Judging from their curve shapes, the UV–vis absorption spectrum (A) of mw-ms-g-C<sub>3</sub>N<sub>4</sub> can be seen as a superimposition of the er-ms-g-C<sub>3</sub>N<sub>4</sub> (B) and mw-g-C<sub>3</sub>N<sub>4</sub> (D) samples.

The photoluminescence (PL) spectra of the g-C<sub>3</sub>N<sub>4</sub> samples obtained are shown in Fig. 8b. We can see that the samples of er-g-C<sub>3</sub>N<sub>4</sub> and mw-g-C<sub>3</sub>N<sub>4</sub> show a strong intrinsic PL peak at ~464 nm, while the mw-ms-g-C<sub>3</sub>N<sub>4</sub> sample presents the lowest intensity in PL spectra. The density of the PL emission spectra can be seen as a scale to measure the degree of recombination of photo-generated electron-hole pairs [45]. The lower the PL intensity indicates the less recombination of photo-generated electron-hole pairs, and the less recombination favors in enhancing the photocatalytic HER performance [15]. The PL results well account for the difference of the photocatalytic HER performance (Fig. 2) of the g-C<sub>3</sub>N<sub>4</sub> samples.

For better understanding the transfer of the photogenerated charge carriers, we characterized the g-C<sub>3</sub>N<sub>4</sub> samples using the time-resolved transient PL decay (TR-PL) spectra, excited by a 370 nm laser and probed at 460 nm, to probe the lifetime of the photo-excited charge carriers [61,62]. Typical TR-PL spectra of the 4 g-C<sub>3</sub>N<sub>4</sub> samples (i.e., mw-ms-g-C<sub>3</sub>N<sub>4</sub>, er-ms-g-C<sub>3</sub>N<sub>4</sub>, er-g-C<sub>3</sub>N<sub>4</sub> and mw-g-C<sub>3</sub>N<sub>4</sub>) are shown in Fig. 8c. Their corresponding radiative lifetimes with different percentages are shown in Table 2. Lifetime  $\tau_1$  is according to free excitons recombination, while  $\tau_2$  and  $\tau_3$  are

**Table 2**

Summary of the analyses of the time-resolved transient PL decay spectra of the g-C<sub>3</sub>N<sub>4</sub> samples.

Sample	$\tau_1$ (ns)	$A_1$ (%)	$\tau_2$ (ns)	$A_2$ (%)	$\tau_3$ (ns)	$A_3$ (%)	$\tau$ (ns)
mw-ms-g-C <sub>3</sub> N <sub>4</sub>	1.90	29.28	9.33	10.92	0.16	59.81	1.67
er-ms-g-C <sub>3</sub> N <sub>4</sub>	2.82	26.87	0.67	64.29	17.94	8.35	2.68
er-g-C <sub>3</sub> N <sub>4</sub>	3.28	50.7	0.73	27.27	13.04	22.03	4.74
mw-g-C <sub>3</sub> N <sub>4</sub>	3.42	50.54	0.54	20.56	14.08	28.90	5.91

caused by non-radiative recombination which are attributed by detrapping of charge carriers [63]. Their relaxation can be described by three time constants:  $\tau_1$ ,  $\tau_2$  and  $\tau_3$  (Table 2). The weighted average recovery lifetimes are 1.67, 2.68, 4.74 and 5.91 ns for mw-ms-g-C<sub>3</sub>N<sub>4</sub>, er-ms-g-C<sub>3</sub>N<sub>4</sub>, er-g-C<sub>3</sub>N<sub>4</sub> and mw-g-C<sub>3</sub>N<sub>4</sub>, respectively. It is well known that the average recovery lifetime can be regarded as a rational measure for evaluating the efficiency of photogenerated electron–hole separation involved in the investigated system [61,62]. The lifetime (1.67 ns) of mw-ms-g-C<sub>3</sub>N<sub>4</sub> is shorter than those of the other samples (i.e., er-ms-g-C<sub>3</sub>N<sub>4</sub>, er-g-C<sub>3</sub>N<sub>4</sub> and mw-g-C<sub>3</sub>N<sub>4</sub>). When considering the photocatalytic HER performance (Table 1), one can find that the shorter the lifetime, the larger the H<sub>2</sub> photo-generation rate. This trend can be understood that a decreased lifetime is resulted from the formation of a special channel of electron transfer. The heterojunctions the triazine-based g-C<sub>3</sub>N<sub>4</sub> and heptazine-based g-C<sub>3</sub>N<sub>4</sub> phases may well account for the shorter lifetime of PL and higher photocatalytic HER performance

According to the UV-vis, PL and TR-PL spectra (Fig. 8), the mw-ms-g-C<sub>3</sub>N<sub>4</sub> sample is of the highest absorption in the range of UV–460 nm and shows the lowest PL peak emission among the as-obtained g-C<sub>3</sub>N<sub>4</sub> samples. Both of the highest absorption and lowest PL emission favor in enhancing its photocatalytic HER performance. According to the results of XPS, EA and XRD, the mw-ms-g-C<sub>3</sub>N<sub>4</sub> sample is composed of a hybrid structure of isotype triazine-/heptazine based g-C<sub>3</sub>N<sub>4</sub> heterojunctions, which account for the lowest PL emission and less recombination of photo-generated electron-hole pairs. Therefore, the formation of isotype triazine-/heptazine based g-C<sub>3</sub>N<sub>4</sub> heterojunction is the key point to improve photocatalytic HER performance.

To determine the bandgap structure of the heptazine-based g-C<sub>3</sub>N<sub>4</sub> and triazine-based g-C<sub>3</sub>N<sub>4</sub> phases, we calculated the conduction bands (CB) of the er-g-C<sub>3</sub>N<sub>4</sub> sample (i.e., heptazine-based g-C<sub>3</sub>N<sub>4</sub>) and the er-ms-g-C<sub>3</sub>N<sub>4</sub> sample (i.e., triazine-based g-C<sub>3</sub>N<sub>4</sub>), according to the Mott-Schottky equation (Eq. (2)):

$$C_{SC}^{-2} = \frac{2(|E - E_{fb}| - kT/e)}{\epsilon \epsilon_r N} \quad (2)$$

where  $e$  is the electron charge of  $1.602 \times 10^{-19}$  C,  $\epsilon_r$  is the relative permittivity,  $\epsilon$  is the vacuum permittivity,  $N$  is the carrier density,  $E$  is the applied bias at the electrode, and  $E_{fb}$  is the flat band potential of a semiconductor (e.g., g-C<sub>3</sub>N<sub>4</sub>) [29,54]. The Mott-Schottky plots and their corresponding linear fits of the triazine-based g-C<sub>3</sub>N<sub>4</sub> (er-ms-g-C<sub>3</sub>N<sub>4</sub>) and heptazine-based g-C<sub>3</sub>N<sub>4</sub> (er-g-C<sub>3</sub>N<sub>4</sub>) samples are shown in Fig. 9. As Fig. 9a shows, both of the Mott-Schottky plots show positive slopes, suggesting the two samples are n-type semiconductors with electrons as the majority carriers. The flat band potentials ( $E_{fb}$ ) of the samples can be estimated by extrapolating their linear fits to  $1/C^2 = 0$ , and give  $-0.90$  V and  $-0.122$  V for the samples of triazine-based g-C<sub>3</sub>N<sub>4</sub> (er-ms-g-C<sub>3</sub>N<sub>4</sub>) and heptazine-based g-C<sub>3</sub>N<sub>4</sub> (er-g-C<sub>3</sub>N<sub>4</sub>), respectively. As Fig. 9b shows, the heptazine-based g-C<sub>3</sub>N<sub>4</sub> (er-g-C<sub>3</sub>N<sub>4</sub>) has a smaller slope than the triazine-based g-C<sub>3</sub>N<sub>4</sub> (er-ms-g-C<sub>3</sub>N<sub>4</sub>), suggesting that the triazine-based g-C<sub>3</sub>N<sub>4</sub> sample has a higher carrier density and much faster carrier transfer, agreeing with the photoelectrochemical results (Figs. 2 and 8). According to the Mott-Schottky results

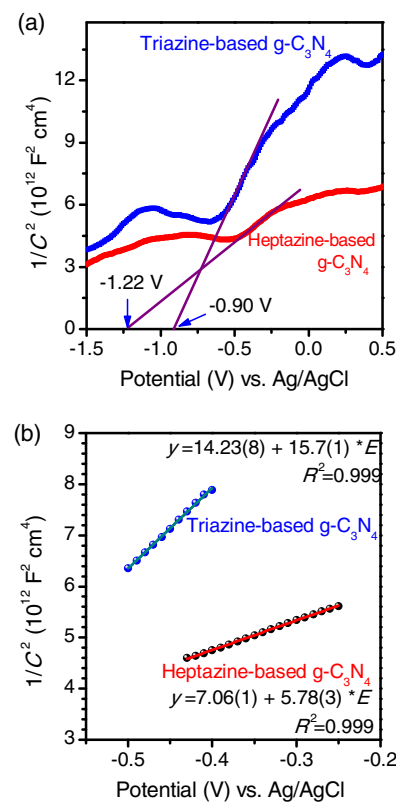
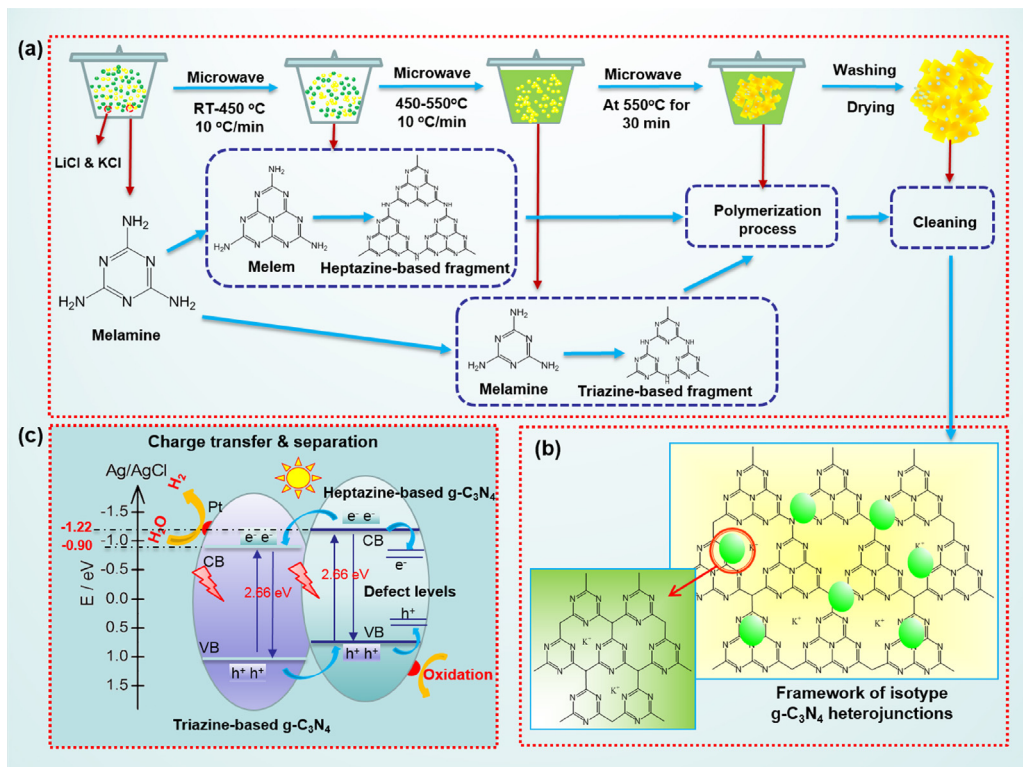


Fig. 9. (a) Mott-Schottky plots of triazine-based g-C<sub>3</sub>N<sub>4</sub> (er-ms-g-C<sub>3</sub>N<sub>4</sub>) and heptazine-based g-C<sub>3</sub>N<sub>4</sub> (er-g-C<sub>3</sub>N<sub>4</sub>); (b) Linear fit plots of the linear parts of Mott-Schottky plots.

(Fig. 9), the conduction bands can be estimated at about  $-1.22$  eV and  $-0.90$  eV for the heptazine-based g-C<sub>3</sub>N<sub>4</sub> phase and triazine-based g-C<sub>3</sub>N<sub>4</sub> phase, respectively. Combining with their bandgap data ( $E_g = 2.66$  eV) determined by their UV-vis spectra (Fig. 8a), one can calculate their valence bands, and the valence bands (i.e., VB) of the heptazine-based g-C<sub>3</sub>N<sub>4</sub> and triazine-based g-C<sub>3</sub>N<sub>4</sub> samples are  $1.44$  and  $1.76$  eV, respectively.

Fig. 10a schematically describes the possible formation mechanism of the isotype triazine-/heptazine based g-C<sub>3</sub>N<sub>4</sub> heterojunction during the microwave-assisted molten-salt process using melamine as the single-source precursor. The formation process can be divided into three stages. At the first step (RT–450 °C,  $10^\circ\text{C min}^{-1}$ ), some melamine molecules sublime and polymerize to form polymeric melem species. The sublimation point of melamine is  $\sim 335$  °C, and it can form polymeric melem at 389 °C [5]. The melting point of the eutectic KCl/LiCl mixture (49.4:50.6 in molar ratio) is about 450 °C, below which the eutectic mixture is still a solid-state phase. The melamine molecules and the newly-formed melem species are therefore confined in the isolated microcells in the solid KCl/LiCl mixture. At the second step (450–550 °C,  $10^\circ\text{C min}^{-1}$ ), the solid KCl/LiCl mixture begins to melt and then provides a special high-temperature liquid media to improve the polymerization reaction of unreacted melamine for the formation of triazine-based fragments. At the third step (550 °C for 30 min), the polymerization reactions of the heptazine-based fragments and triazine-based fragments continue and finally form the isotype triazine-/heptazine based g-C<sub>3</sub>N<sub>4</sub> heterojunctions. During the rapid heating of microwave irradiation, some melamine molecules tend to form polymeric melem [53] at the temperature below 450 °C, while the others tend to form the triazine-based g-C<sub>3</sub>N<sub>4</sub> species. The newly formed triazine-based g-C<sub>3</sub>N<sub>4</sub> and heptazine-based g-C<sub>3</sub>N<sub>4</sub> species can be easily connected



**Fig. 10.** (a) Possible formation mechanism of isotype triazine-/heptazine based  $\text{g-C}_3\text{N}_4$  heterojunctions in microwave-assisted molten-salt process; (b) Schematic expression of the isotype  $\text{g-C}_3\text{N}_4$  heterojunctions; (c) Possible routes for the separation of photogenerated electron-hole pairs and their transfer in the sotype triazine-/heptazine based  $\text{g-C}_3\text{N}_4$  heterojunctions.

with one another at the molecular level in the confined liquid phase of molten KCl/LiCl (Fig. 10b). For charge balance, some K<sup>+</sup> ions can be embedded in the voids or spacings of the carbon nitride layers (Fig. 10b). It is worth to note that the molten salt (KCl/LiCl) plays multiple roles: (1) to act as microcells that hinder the agglomeration at the initial polycondensation [12–14]; (2) to offer a special ionic liquid media that favors in the formation of triazine-based units and results in the co-existence of melamine and melem units; (3) to accelerate the absorption of microwave radiation and to achieve a rapid synthesis; (4) to promote the formation of isotype triazine-/heptazine based  $\text{g-C}_3\text{N}_4$  heterojunctions in a one-pot process using a single-source precursor.

Taking chemical compositions, microstructures and formation process into account, we can conclude the possible reasons why the mw-ms- $\text{g-C}_3\text{N}_4$  sample has a higher photocatalytic HER activity than the other  $\text{g-C}_3\text{N}_4$  samples. First of all, the mw-ms- $\text{g-C}_3\text{N}_4$  sample consists of the isotype triazine-/heptazine based  $\text{g-C}_3\text{N}_4$  heterojunction with a unique electric band structure of type II heterojunction (Fig. 10c), which can provides a more convenient path for the transfer of photo-generated carriers and lead to more efficient separation of photo-generated electron-hole pairs than the other  $\text{g-C}_3\text{N}_4$  samples obtained [55,56]. Secondly, some defects formed in the mw-ms process, e.g., N vacancies and K<sup>+</sup> ions adsorbed, can trap carries to further improve the separation of photo-generated electron-hole pairs. Thirdly, the thin two-dimensional plate-like morphology (Fig. 6) of the heptazine-/triazine-based  $\text{g-C}_3\text{N}_4$  heterojunctions can shorten the transmission distance and then decrease the recombination probability of the photo-generated electron-hole pairs [15]. Finally, the excellent dispersibility of mw-ms- $\text{g-C}_3\text{N}_4$  in water (Fig. S3, ESI†) provides a closer contact with reactants and then enhances its photocatalytic HER performance.

Stability and recycling performance of the mw-ms- $\text{g-C}_3\text{N}_4$  sample is shown in Fig. 11a. One can find that the HER performance of the mw-ms- $\text{g-C}_3\text{N}_4$  photocatalyst has no obvious deactivation after being illuminated for 12 h under visible light, indicating that the  $\text{g-C}_3\text{N}_4$  photocatalyst obtained via the microwave-assisted molten-salt process are stable in the present condition. To further corroborate the stability of the mw-ms- $\text{g-C}_3\text{N}_4$  photocatalyst, we characterized the re-collected solids after the HER experiment using the XRD technique (Fig. S14, ESI†). One can find that the XRD patterns before and after the photocatalytic HER test are similar, suggesting that there is no obvious change in their phase structure during the HER process.

To check the universality of the photocatalytic effect, we used the  $\text{g-C}_3\text{N}_4$  samples to photo-degrade organic dyes under visible-light irradiation ( $\lambda > 420 \text{ nm}$ ). Fig. 11b shows the UV-vis spectra of the RhB aqueous solutions after photodegradation for various times (0–60 min). It is clear that the intensity of the characteristic RhB peak at 551 nm decreases with the increase in the photodegradation time, and the location of the characteristic peak of RhB is not significantly changed. Fig. 11c compares the photodegradation behavior of the  $\text{g-C}_3\text{N}_4$  samples synthesized by various processes, and Fig. 11d shows their corresponding photodegradation rates ( $k, \text{min}^{-1}$ ). One can find that the sample of mw-ms- $\text{g-C}_3\text{N}_4$  is of the highest rate for RhB photodegradation. Therefore the mw-ms- $\text{g-C}_3\text{N}_4$  sample is of stable and universal photocatalytic performance, e.g., photocatalytic HER and organic degradation.

To check the generality and practicability of the microwave-assisted molten-salt process in the synthesis of  $\text{g-C}_3\text{N}_4$  photocatalysts, we designed a series of synthesis using KCl/LiCl mixture with various melting points (353, 400 and 450 °C) at different polymerization temperatures (520, 550 and 580 °C) for various times (15, 30 and 45 min). The XRD, FT-IR, UV-vis DR spectra (Fig. S4 and S6, ESI†) indicate that the samples obtained at 550 °C for

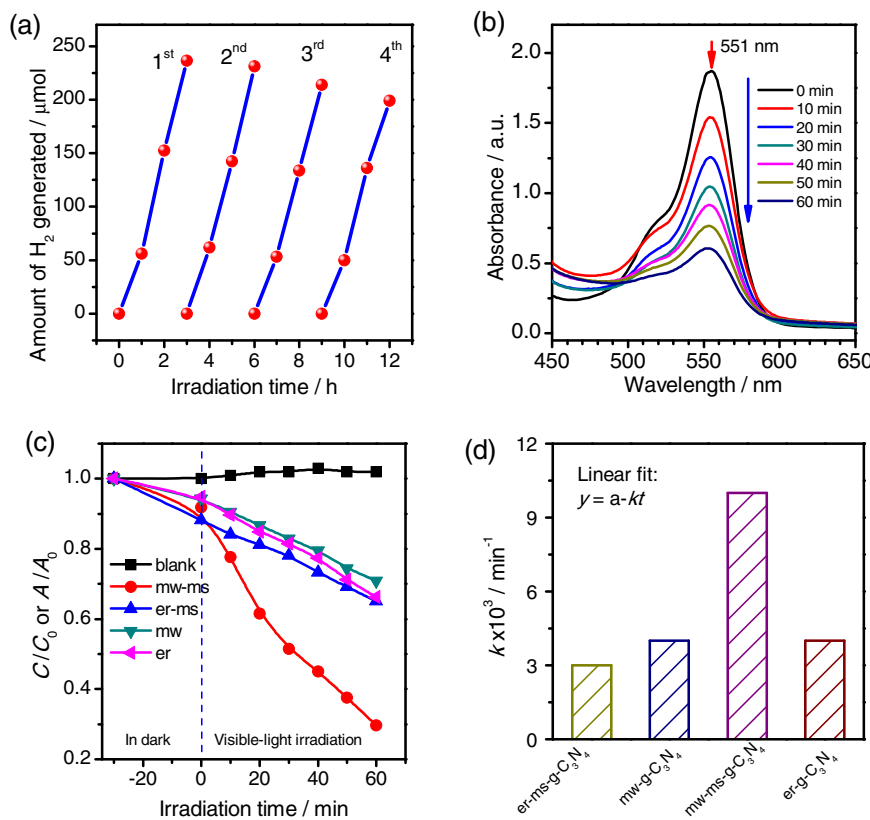


**Fig. 11.** (a) Stability and recycling hydrogen evolution activity of the g-C<sub>3</sub>N<sub>4</sub> sample (mw-ms-g-C<sub>3</sub>N<sub>4</sub>) obtained via the microwave-assisted molten-salt process; (b) Typical UV-vis spectra of RhB aqueous solutions after photocatalytic degradation for various times using mw-ms-g-C<sub>3</sub>N<sub>4</sub> as the photocatalyst (50 mg photocatalyst in 50 mL of 10 mg L<sup>-1</sup> RhB solution under visible-light irradiation,  $\lambda > 420$  nm); (c-d) Comparison of the photocatalytic RhB degradation activity of the g-C<sub>3</sub>N<sub>4</sub> photocatalysts obtained via different processes.

30 min using KCl/LiCl mixtures with various melting points are of a similar phase and chemical composition. The photocatalytic tests (Fig. S7, ESI†) indicate that the samples obtained with the molten salts with higher melting points (400 and 450 °C) have higher HER activities than the sample obtained with lower melting-point molten salt (353 °C). Reaction temperatures in the mw-ms process also have effects on the HER property of g-C<sub>3</sub>N<sub>4</sub> samples. The g-C<sub>3</sub>N<sub>4</sub> sample obtained at 550 °C has a higher HER activity than the samples obtained at 520 and 580 °C (Fig. S8 and S9, ESI†). In addition, microwave-irradiation time in the mw-ms synthesis has some influence on their photocatalytic HER performance. Under the synthetic conditions with molten salts (m.p. 450 °C) at 550 °C for various times, the g-C<sub>3</sub>N<sub>4</sub> sample obtained for 30 min shows a higher HER activity than the samples obtained for 15 min or 45 min (Fig. S10 and S11, ESI†). Therefore, the optimum conditions for the synthesis of g-C<sub>3</sub>N<sub>4</sub> samples via the mw-ms process are 550 °C for 30 min using a molten salt of KCl/LiCl with a melting point of 450 °C as the polymerization media. It is worth to note that although the synthetic conditions influence the photocatalytic HER performance, the fluctuation in their HER activity is not so obvious, and the microwave-assisted molten-salt process is therefore a robust approach to synthesize high-performance g-C<sub>3</sub>N<sub>4</sub> photocatalysts for HER applications.

To check the effect of heterojunctions between triazine-based g-C<sub>3</sub>N<sub>4</sub> and heptazine-based g-C<sub>3</sub>N<sub>4</sub> phases on photocatalytic activity, we made a mixture consisting of triazine-based g-C<sub>3</sub>N<sub>4</sub>/heptazine-based g-C<sub>3</sub>N<sub>4</sub> phases by physically mixing the er-g-C<sub>3</sub>N<sub>4</sub> and er-ms-g-C<sub>3</sub>N<sub>4</sub> (1:1 in mass ratio). The XRD pattern and FT-IR spectra of the mixture are similar to those of the mw-ms-g-C<sub>3</sub>N<sub>4</sub> sample (Fig. S13, ESI†). However, the photocatalytic RhB degradation activity (Fig. S12, ESI†) of the mixture is much

lower than that of the mw-ms-g-C<sub>3</sub>N<sub>4</sub> sample, suggesting that the heterojunctions between the triazine-based g-C<sub>3</sub>N<sub>4</sub> and heptazine-based g-C<sub>3</sub>N<sub>4</sub> phases are essentially important in improving their photocatalytic performance.

Table 3 compares the microwave-assisted molten-salt process with some recently reported methods in the synthesis and HER performance of g-C<sub>3</sub>N<sub>4</sub> photocatalysts using melamine as the single-source precursor. One can find that the microwave-assisted molten-salt process developed here is of some outstanding advantages: rapid synthesis, high yield, simple process, and high photocatalytic HER performance.

#### 4. Conclusions

The unique isotype heterojunctions of triazine-based g-C<sub>3</sub>N<sub>4</sub>/heptazine-based g-C<sub>3</sub>N<sub>4</sub> have been synthesized by a newly-developed microwave-assisted molten-salt (mw-ms) process using melamine as the single-source precursor for the first time. The mw-ms process combined the advantages of rapid heating of microwave irradiation and high-temperature liquid media of molten salt (KCl/LiCl), which provide a unique condition for the one-pot rapid synthesis of isotype triazine-/heptazine based g-C<sub>3</sub>N<sub>4</sub> heterojunctions. The typical isotype g-C<sub>3</sub>N<sub>4</sub> heterojunction (55 wt.% in yield) has been synthesized at 550 °C for 30 min, and shows a visible-light driven photocatalytic HER rate of 1480  $\mu\text{mol g}^{-1} \text{h}^{-1}$ , which is 5 times that (300  $\mu\text{mol g}^{-1} \text{h}^{-1}$ ) of the er-ms-g-C<sub>3</sub>N<sub>4</sub> sample, 15 times that (95  $\mu\text{mol g}^{-1} \text{h}^{-1}$ ) of the er-g-C<sub>3</sub>N<sub>4</sub> sample and 23 times that (63  $\mu\text{mol g}^{-1} \text{h}^{-1}$ ) of the mw-g-C<sub>3</sub>N<sub>4</sub> sample. The typical AQY at 420 nm of the isotype g-C<sub>3</sub>N<sub>4</sub> heterojunction is as high as 10.7%. The huge enhancement in HER activity should be attributed to the isotype triazine-/heptazine based g-

**Table 3**Comparison of the synthesis and HER performance of g-C<sub>3</sub>N<sub>4</sub> photocatalysts using melamine as the single-source precursor.

Synthetic process	Yield <sup>a</sup>	Photocatalytic HER performance	Microstructure	Reference
Thermal polymerization with H <sub>2</sub> SO <sub>4</sub> pre-treatment (at 600 °C for 4 h in Ar)	<15 wt%	220 μmol g <sup>-1</sup> h <sup>-1</sup> (0.5 wt.% Pt-loading, 10 vol.% TEOA solution, λ > 420 nm)	Bulk	[57]
Thermal polymerization (at 550 °C for 2 h in air)	N/A <sup>b</sup>	355 μmol g <sup>-1</sup> h <sup>-1</sup> (1 wt.% Pt-loading, 80 vol.% methanol solution, λ > 400 nm)	Nanosheets & aggregation	[49]
Molten salt method (at 550 °C for 4 h in air)	N/A	880 μmol g <sup>-1</sup> h <sup>-1</sup> (3 wt.% Pt-loading, 10 vol.% TEOA solution, λ > 420 nm)	Nanosheets & aggregation	[44]
Thermal polymerization (at 400 °C for 1.5 h in air and at 700 °C for 2 h in N <sub>2</sub> )	N/A	3450 μmol g <sup>-1</sup> h <sup>-1</sup> (3 wt.% Pt-loading, 10 vol.% TEOA solution, visible-light)	Nanosheets & aggregation	[58]
Microwave heating (1000 W for 18 min, >1000 °C, closed container)	33%	200 ~ 250 μmol g <sup>-1</sup> h <sup>-1</sup> (0.5 wt.% Pt-loading, 15 vol% TEOA solution, λ > 420 nm)	N/A	[39]
Thermal polymerization (at 450–520 °C for 2 h; and at 470–540 °C for 2 h in Air)	~40.7%	689 μmol g <sup>-1</sup> h <sup>-1</sup> (3 wt.% Pt-loading, 15 vol% TEOA solution, λ > 420 nm)	Nanorods & aggregation	[59]
Microwave-assisted molten-salt process (at 550 °C for 15–30 min in air)	54–62%	1480 μmol g <sup>-1</sup> h <sup>-1</sup> (3 wt.% Pt-loading, 10 vol.% TEOA solution, λ > 420 nm)	Nanosheets	this work

<sup>a</sup> The mass ratio of obtained solid to its precursor.<sup>b</sup> Not available.

C<sub>3</sub>N<sub>4</sub> heterojunctions with a suitable configuration in electronic band structures, which provides efficient paths for transport and separation of photo-generated electron-hole pairs. The synergistic effects of microwave heating and molten-salt liquid polycondensation condition provide a robust platform for rapid synthesis of g-C<sub>3</sub>N<sub>4</sub> based HER photocatalysts. The mw-ms process is potential method for large-scale synthesis of g-C<sub>3</sub>N<sub>4</sub> based HER photocatalysts and other extended material systems.

## Acknowledgments

This work was partly sponsored by National Natural Science Foundation of China (NSFC no. 51172211, 51574205), China Postdoctoral Science Foundation (2013M531682, 2014T70682), Program for Science & Technology Innovation Talents in Universities of Henan Province (14HASTIT011), Special Support Program for High-End Talents of Zhengzhou University (ZDGD13001), Program from Dongguan University of Technology (G200906-17), and Plan for Scientific Innovation Talent of Henan Province (154100510003). The authors thank Prof. Shuangquan Zang (Zhengzhou University), Mr. Jie Zhang (Zhengzhou University), Mr. Renwu Huang (Zhengzhou University), Miss Bing Ma (Zhengzhou University), Mr. Pengfei Wang (Nankai University), and Miss Ziwei Pan (University of Science and Technology of China) for their kind help in measuring PL spectra and Mott-Schottky plots.

## Appendix A. Supplementary data

Supplementary data associated with this article can be found, in the online version, at <http://dx.doi.org/10.1016/j.apcatb.2016.10.014>.

## References

- [1] Z. Zhao, Y. Sun, F. Dong, *Nanoscale* 7 (2015) 15–37.
- [2] X. Chen, S. Shen, L. Guo, S.S. Mao, *Chem. Rev.* 110 (2010) 6503–6570.
- [3] K. Iwashina, A. Iwase, Y.H. Ng, R. Amal, A. Kudo, *J. Am. Chem. Soc.* 137 (2015) 604–607.
- [4] C. Liu, L. Wang, Y. Tang, S. Luo, Y. Liu, S. Zhang, Y. Zeng, Y. Xu, *Appl. Catal. B* 164 (2015) 1–9.
- [5] X. Wang, K. Maeda, A. Thomas, K. Takanabe, G. Xin, J.M. Carlsson, K. Domen, M. Antonietti, *Nat. Mater.* 8 (2009) 76–80.
- [6] Y. Wang, X. Wang, M. Antonietti, *Angew. Chem. Int. Ed.* 51 (2012) 68–89.
- [7] A. Zambon, J.M. Mouesca, C. Gheorghiu, P.A. Bayle, J. Pécaut, M. Claeys-Bruno, S. Gambarelli, L. Dubois, *Chem. Sci.* 7 (2016) 945–950.
- [8] D.J. Martin, K. Qiu, S.A. Shevlin, A.D. Handoko, X. Chen, Z. Guo, J. Tang, *Angew. Chem. Int. Ed.* 126 (2014) 9394–9399.
- [9] W.J. Ong, L.L. Tan, Y.H. Ng, S.T. Yong, S.P. Chai, *Chem. Rev.* 116 (2016) 7159–7329.
- [10] Y. Hou, A.B. Laursen, J. Zhang, G. Zhang, Y. Zhu, X. Wang, S. Dahl, I. Chorkendorff, *Angew. Chem. Int. Ed.* 52 (2013) 3621–3625.
- [11] H.J. Kong, D.H. Won, J. Kim, S.I. Woo, *Chem. Mater.* 28 (2016) 1318–1324.
- [12] Z. Wang, W. Guan, Y. Sun, F. Dong, Y. Zhou, W.K. Ho, *Nanoscale* 7 (2015) 2471–2479.
- [13] F. He, G. Chen, Y. Yu, Y. Zhou, Y. Zheng, S. Hao, *Chem. Commun.* 51 (2015) 425–427.
- [14] F. He, G. Chen, Y. Zhou, Y. Yu, Y. Zheng, S. Hao, *Chem. Commun.* 51 (2015) 16244–16246.
- [15] P. Yang, J. Zhao, W. Qiao, L. Li, Z. Zhu, *Nanoscale* 7 (2015) 18887–18890.
- [16] Y. Kang, Y. Yang, L.C. Yin, X. Kang, G. Liu, H.M. Cheng, *Adv. Mater.* 27 (2015) 4572–4577.
- [17] Q. Han, F. Zhao, C. Hu, L. Lv, Z. Zhang, N. Chen, L. Qu, *Nano Res.* 8 (2015) 1718–1728.
- [18] Y. Wang, J. Zhang, X. Wang, M. Antonietti, H. Li, *Angew. Chem. Int. Ed.* 49 (2010) 3356–3359.
- [19] X. Fan, L. Zhang, R. Cheng, M. Wang, M. Li, Y. Zhou, J. Shi, *ACS Catal.* 5 (2015) 5008–5015.
- [20] X. Fan, L. Zhang, M. Wang, W. Huang, Y. Zhou, M. Li, R. Cheng, J. Shi, *Appl. Catal. B* 182 (2016) 68–73.
- [21] S. Cao, J. Low, J. Yu, M. Jaroniec, *Adv. Mater.* 27 (2015) 2150–2176.
- [22] H. Li, S. Gan, H. Wang, D. Han, L. Niu, *Adv. Mater.* 27 (2015) 6906–6913.
- [23] Z. Zhu, Z. Lu, D. Wang, X. Tang, Y. Yan, W. Shi, Y. Wang, N. Gao, X. Yao, H. Dong, *Appl. Catal. B* 182 (2016) 115–122.
- [24] D.J. Martin, P.J. Reardon, S.J. Moniz, J. Tang, *J. Am. Chem. Soc.* 136 (2014) 12568–12571.
- [25] F. Dong, Z. Zhao, T. Xiong, Z. Ni, W. Zhang, Y. Sun, W.K. Ho, *ACS Appl. Mater. Interfaces* 5 (2013) 11392–11401.
- [26] J. Liu, Y. Liu, N. Liu, Y. Han, X. Zhang, H. Huang, Y. Lifshitz, S.T. Lee, J. Zhong, Z. Kang, *Science* 347 (2015) 970–974.
- [27] Z. Tong, D. Yang, J. Shi, Y. Nan, Y. Sun, Z. Jiang, *ACS Appl. Mater. Interfaces* 7 (2015) 25693–25701.
- [28] Y. Zhao, J. Zhang, L. Qu, *ChemNanoMat* 1 (2015) 298–318.
- [29] J. Zhang, M. Zhang, R.Q. Sun, X. Wang, *Angew. Chem. Int. Ed.* 51 (2012) 10145–10149.
- [30] M.J. Bojdys, J.O. Muller, M. Antonietti, A. Thomas, *Chem. Eur. J.* 14 (2008) 8177–8182.
- [31] K. Schwinghammer, B. Tuffy, M.B. Mesch, E. Wirnhier, C. Martineau, F. Taulelle, W. Schnick, J. Senker, B.V. Lotsch, *Angew. Chem. Int. Ed.* 52 (2013) 2435–2439.
- [32] M.K. Bhunia, S. Melissen, M.R. Parida, P. Sarawade, J.-M. Basset, D.H. Anjum, O.F. Mohammed, P. Sautet, T. Le Bahers, K. Takanabe, *Chem. Mater.* 27 (2015) 8237–8247.
- [33] D. Dontsova, S. Pronkin, M. Wehle, Z. Chen, C. Fettkenhauer, G. Clavel, M. Antonietti, *Chem. Mater.* 27 (2015) 5170–5179.
- [34] D. Dontsova, C. Fettkenhauer, V. Papaefthimiou, J. Schmidt, M. Antonietti, *Chem. Mater.* 28 (2016) 772–778.
- [35] N. Fechler, N.P. Zussblatt, R. Rothe, R. Schlögl, M.-G. Willinger, B.F. Chmelka, M. Antonietti, *Adv. Mater.* 28 (2016) 1287–1294.
- [36] X. Liu, C. Giordano, M. Antonietti, *Small* 10 (2014) 193–200.
- [37] B. Liu, H.M. Chen, C. Liu, S.C. Andrews, C. Hahn, P. Yang, J. Am. Chem. Soc. 135 (2013) 9995–9998.
- [38] I. Bilecka, M. Niederberger, *Nanoscale* 2 (2010) 1358.
- [39] Y.P. Yuan, L.S. Yin, S.W. Cao, L.N. Gu, G.S. Xu, P. Du, H. Chai, Y.S. Liao, C. Xue, *Green Chem.* 16 (2014) 4663–4668.
- [40] Y.J. Zhu, F. Chen, *Chem. Rev.* 114 (2014) 6462–6555.
- [41] L. Yin, D. Chen, M. Hu, H. Shi, D. Yang, B. Fan, G. Shao, R. Zhang, G. Shao, *J. Mater. Chem. A* 2 (2014) 18867–18874.
- [42] Z. Xuan, Y. Shiyue, L. Yumei, W. Zuoshan, L. Weifeng, *Mater. Lett.* 145 (2015) 23–26.

- [43] L. Xiao, H. Shen, R. von Hagen, J. Pan, L. Belkoura, S. Mathur, *Chem. Commun.* 46 (2010) 6509–6511.
- [44] M.K. Bhunia, K. Yamauchi, K. Takanabe, *Angew. Chem. Int. Ed.* 53 (2014) 11001–11005.
- [45] D. Jiang, J. Li, C. Xing, Z. Zhang, S. Meng, M. Chen, *ACS Appl. Mater. Interfaces* 7 (2015) 19234–19242.
- [46] X. Lu, K. Xu, P. Chen, K. Jia, S. Liu, C. Wu, *J. Mater. Chem. A* 2 (2014) 18924–18928.
- [47] P. Niu, L. Zhang, G. Liu, H.-M. Cheng, *Adv. Funct. Mater.* 22 (2012) 4763–4770.
- [48] Q. Tay, P. Kanhere, C.F. Ng, S. Chen, S. Chakraborty, A.C.H. Huan, T.C. Sum, R. Ahuja, Z. Chen, *Chem. Mater.* 27 (2015) 4930–4933.
- [49] S. Martha, A. Nashim, K.M. Parida, *J. Mater. Chem. A* 1 (2013) 7816.
- [50] Q. Liang, Z. Li, Z.H. Huang, F. Kang, Q.H. Yang, *Adv. Funct. Mater.* 25 (2015) 6885–6892.
- [51] Q. Han, B. Wang, J. Gao, Z. Cheng, Y. Zhao, Z. Zhang, L. Qu, *ACS Nano* 10 (2016) 2745–2751.
- [52] Y.P. Zhu, T.Z. Ren, Z.Y. Yuan, *ACS Appl. Mater. Interfaces* 7 (2015) 16850–16856.
- [53] E. Wirnhier, M. Doblinger, D. Gunzelmann, J. Senker, B.V. Lotsch, W. Schnick, *Chem. Eur. J.* 17 (2011) 3213–3221.
- [54] C. Zhao, H. Luo, F. Chen, P. Zhang, L. Yi, K. You, *Energy Environ. Sci.* 7 (2014) 1700.
- [55] J. Zhang, X. Chen, K. Takanabe, K. Maeda, K. Domen, J.D. Epping, X. Fu, M. Antonietti, X. Wang, *Angew. Chem. Int. Ed.* 49 (2010) 441–444.
- [56] J. Zhang, J. Sun, K. Maeda, K. Domen, P. Liu, M. Antonietti, X. Fu, X. Wang, *Energy Environ. Sci.* 4 (2011) 675–678.
- [57] H. Yan, Y. Chen, S. Xu, *Int. J. Hydrogen Energy* 37 (2012) 125–133.
- [58] Y. Chen, B. Wang, S. Lin, Y. Zhang, X. Wang, *J. Phys. Chem. C* 118 (2014) 29981–29989.
- [59] Q. Gu, Z. Gao, H. Zhao, Z. Lou, Y. Liao, C. Xue, *RSC Adv.* 5 (2015) 49317–49325.
- [60] L. Lin, H. Ou, Y. Zhang, X. Wang, *ACS Catal.* 6 (2016) 3921–3931.
- [61] L. Wang, X. Duan, G. Wang, C. Liu, S. Luo, S. Zhang, Y. Zeng, Y. Xu, Y. Liu, X. Duan, *Appl. Catal. B* 186 (2016) 88–96.
- [62] X. Li, W. Bi, L. Zhang, S. Tao, W. Chu, Q. Zhang, Y. Luo, C. Wu, Y. Xie, *Adv. Mater.* 28 (2016) 2427–2431.
- [63] Z. Sun, H. Zheng, J. Li, P. Du, *Energy Environ. Sci.* 8 (2015) 2668–2676.
- [64] G. Zhang, M. Zhang, X. Ye, X. Qiu, S. Lin, X. Wang, *Adv. Mater.* 26 (2014) 805–809.
- [65] S. Guo, Z. Deng, M. Li, B. Jiang, C. Tian, Q. Pan, H. Fu, *Angew. Chem. Int. Ed.* 55 (2016) 1830–1834.
- [66] G. Liu, T. Wang, H. Zhang, X. Meng, D. Hao, K. Chang, P. Li, T. Kako, J. Ye, *Chem. Int. Ed.* 54 (2015) 1–6.